

Analysis of the surface hydrology of the
Greenland Ice Sheet using
Sentinel-1 Synthetic Aperture Radar



Katharine E. Miles

Scott Polar Research Institute
University of Cambridge

Lucy Cavendish College

This dissertation is submitted for the degree of

Master of Philosophy

2016

Declaration

The dissertation submitted is entirely my own work, and includes nothing that is the outcome of work done in collaboration with others, except where clearly acknowledged in the text or Acknowledgements. It has not been submitted in whole or in part for a degree at this, or any other University. This dissertation does not exceed 20,000 words, excluding Figures and their captions, Tables and their captions, the Cover Page, Declaration, Acknowledgements, Appendices, References, Table of Contents and List of Figures and Tables.

Signed:

Date:

Acknowledgements

- To my supervisor, Dr. Ian Willis (Scott Polar Research Institute) for providing the initial opportunity to research this topic, and for his support and insights throughout the year.

- To Corinne Benedek (Scott Polar Research Institute) and Marco Tedesco (Columbia University) for allowing me to pursue this topic as a complementary, but discrete research project to Corinne's PhD thesis, and for their support regarding the initial processing and specifics of the Sentinel data. Particular thanks go to Corinne, without whom I would not have been able to carry out this research.

- To Andrew Williamson (Scott Polar Research Institute), who provided the rapid drainage detection algorithm and greatly assisted in its successful outputs, as well as unfaltering advice on multiple sections of the methodology.

- To Dr. Neil Arnold (Scott Polar Research Institute) for his advice regarding the dilation of the Landsat lake mask, and to Dr. Gareth Rees (Scott Polar Research Institute) for his advice regarding the dual polarisations of the Sentinel data.

- To Dr. Poul Christoffersen and Dr. Gareth Rees (Scott Polar Research Institute) for granting the extension to my dissertation deadline, and to my Tutor, Dr. Sue Jackson (Lucy Cavendish College), for supporting me through this process.

- Finally, thanks go to everyone who helped me through this year, including the jazz bands (ChuJazz and CUJO), and the other SPRI MPhils for a fantastic year of Polar Studies - particularly Sarah W. Cooley for her camaraderie, encouragement, and our seemingly never-ending discussions on supraglacial lakes.

Abstract

Surface meltwater on the Greenland Ice Sheet (GrIS) has recently received much attention due to its ability to pond to form features such as firn slush zones and supraglacial lakes. This study uses imagery from the recently launched Sentinel-1 Synthetic Aperture Radar sensors to investigate supraglacial lakes in southwest Greenland. This novel method can overcome some of the limitations of optical sensors that are more commonly used for investigations of the surface hydrology of the GrIS, including an inability to image through cloud or in darkness, without compromising either the high temporal or spatial resolution of the imagery. A semi-automated algorithm is developed to detect supraglacial lakes from the Sentinel images during the summer of 2015, which is relatively successful when compared to Landsat NDWI classification of supraglacial lakes. The lake detections are then utilised in a fully-automated rapid lake detection algorithm to investigate supraglacial lake dynamics through the summer (June to September). A total of 48 drainages were detected from the Sentinel data over the ~42,000 km² study site for lakes greater than 0.2 km². The analysis is then extended into the early winter months (October and November), where the Sentinel imagery allows the accurate determination of the date of lake freeze-over; the mean freeze-over date for 300 lakes is DoY 240.1 ± 3.7 days from the Sentinel imagery, which is beyond the limit of useful Landsat scenes available for 2015. Furthermore, the Sentinel imagery has allowed the detection of buried lake areas, as well as the date of buried lake appearance and disappearance, which has not previously been carried out in the literature.

Table of Contents

Statement	2
Acknowledgements	4
Abstract	5
Table of Contents	6
List of Figures and Tables	8
1. Introduction	9
2. Literature Review	12
2.1 – Hydrology of the Greenland Ice Sheet	12
2.1.1 – The Hydrological System	12
2.1.2 – Impact of Hydrology on Ice Motion	15
2.1.3 – Supraglacial Lakes and Ice Motion	17
2.3 – Remote Sensing of Supraglacial Lakes	19
2.3.1 – Optical Imagery	19
2.3.2 – Radar imagery	21
2.3.3 – Sentinel-1	22
3. Methodology	24
3.1 – Study Site	24
3.2 – Methods	25
3.2.1 – Lake Detection	25
3.2.2 – Lake Drainage	32
3.2.3 – Lake Freeze-Over	34
3.2.4 – Buried Lakes	35
4. Results	38
4.1 – Lake Detection	38
4.2 – Lake Drainage	45
4.3 – Lake Freeze-Over	48
4.4 – Buried Lakes	52

5. Discussion	55
5.1 – Lake Detection	55
5.2 – Lake Drainage	60
5.3 – Lake Freeze-Over.....	62
5.4 – Buried Lakes.....	65
6. Conclusions	67
7. References	71

List of Figures and Tables

Figure 1 – Study site location.....	24
Figure 2 – Illustrated processing workflow.....	27
Figure 3 – Sentinel lake detections by each polarisation	31
Figure 4 – Rapid lake drainage examples	33
Figure 5 – Example of Sentinel lakes visible through snowcover.....	35
Figure 6 – Example of buried lakes	36
Figure 7 – Buried lake distribution compared to Koenig et al. (2015, Figure 3)	36
Figure 8 – Examples of the Landsat and Sentinel lake detections	39
Figure 9 – Graph comparing lake areas detected by the Landsat and Sentinel methods.....	40
Figure 10 – Graph showing the difference in the calculated lake areas	41
Figure 11 – Graph displaying the Sentinel polarisation detections of lake areas	42
Figure 12 – Example of problematic lakes for the Sentinel lake detection method	43
Figure 13 – Graph displaying standardised total lake areas from Landsat and Sentinel	44
Figure 14 – Example drainage date detections from Landsat and Sentinel.....	47
Figure 15 – Lake freeze-over date (and errors) detections from Landsat and Sentinel.....	49
Figure 16 – Graph displaying the freeze-over date (and errors) for Landsat and Sentinel.....	51
Figure 17 – Graph displaying buried lake appearance and disappearance (and errors).....	51
Figure 18 – Buried lake appearance and disappearance (and errors) detections.....	53
Table 1 – Landsat images used in the summer lake detections and drainage analysis	26
Table 2 – Sentinel images used in the summer lake detections and drainage analysis.....	26
Table 3 – Lake detection statistics for the Landsat and Sentinel data	39
Table 4 – Drainage detection statistics for the Landsat and Sentinel data	46
Table 5 – Freeze-over detection statistics for the Landsat and Sentinel data	48
Table 6 – Buried lake appearance and disappearance detection statistics	52

1. Introduction

The rate of mass loss of the Greenland Ice Sheet (GrIS) accelerated by $21.9 \pm 1 \text{ Gt yr}^{-2}$ between 1992 and 2009 (Rignot et al. 2011); increasing the average annual mass loss from $243 \pm 18 \text{ Gt yr}^{-1}$ (0.68 mm yr^{-1} sea-level rise) between 2003 and 2009 (Csatho et al. 2014) to $378 \pm 50 \text{ Gt yr}^{-1}$ from 2009-2012 (Enderlin et al. 2014). Prior to 2006, this mass loss was evenly split between surface and dynamical processes, however, since 2006, the contribution of surface melting and runoff has accelerated significantly and now dominates the total mass loss, particularly in the southwest of the ice sheet (van den Broeke et al. 2009; Vaughan et al. 2013). Summer temperatures over the GrIS increased by 1.6°C between 1840 and 2010, enhancing surface meltwater production by 59% (Box 2013), and forcing 84% of the increase in GrIS mass loss since 2009 over a growing proportion of the ice sheet (Vaughan et al. 2013; Enderlin et al. 2014). Meltwater on the surface of the GrIS can form runoff into channels, which either reach the ice sheet edge, drain into moulins or crevasses, or pond into supraglacial lakes, which have been observed to overflow slowly or drain catastrophically (Echelmeyer et al. 1991; Das et al. 2008; Tedesco et al. 2013; Chu 2014). If this meltwater reaches the subglacial drainage system, it may influence ice velocity on diurnal, seasonal or annual timescales, potentially enhancing basal sliding and further accelerating mass loss through increased ice velocities (Zwally et al. 2002; Shepherd et al. 2009; Hoffman et al. 2011; Van de Wal et al. 2015). Additionally, the greater temporal and spatial presence of meltwater across the GrIS during the ablation season resulted in an 18% decrease in surface albedo in coastal regions of the GrIS between 2003 and 2012, allowing more energy to be absorbed for melting and creating a positive feedback between melt production and albedo (Vaughan et al. 2013). However, the precise impact that an intensifying volume of meltwater may have on ice dynamics is currently unknown; some studies suggest that increased melt may actually reduce annual ice velocities (Liang et al. 2012; Sole et al. 2013; Tedstone et al. 2015). With models showing that future GrIS mass loss will be most sensitive to climatic changes (Bindschadler et al. 2013), it is vital that the effect of meltwater on ice dynamics is better understood. Crucial to these processes is the study of the presence and behaviour of supraglacial lakes, from which inferences about their impact on ice dynamics can be made.

Studies of supraglacial lakes have primarily used remote sensing to investigate the presence, distribution, depth, area, volume and lifespan of supraglacial lakes. The main sensors include the optical and infrared wavelengths of the MODerate-resolution Imaging Spectroradiometer (MODIS) (e.g. Box & Ski 2007), which has an extremely high temporal resolution of twice-daily coverage over large swath areas; and the Landsat satellites, which have very high spatial resolutions (30 m for Landsat-8) (e.g. Pope et al. 2016). However, both the 250 m spatial resolution of MODIS and low temporal resolution of Landsat imagery (16-day repeat) (Pope et al. 2016) are less suited to investigating supraglacial lakes, which can be small in size and undergo rapid changes – lakes have been observed to drain in a matter of hours (Das et al. 2008) – potentially resulting in key dynamics being missed. Furthermore, such sensors are unable to image through cloud or in darkness, restricting the number of useful scenes that can be utilised for supraglacial lake studies.

An alternative method is Synthetic Aperture Radar (SAR), a satellite-borne active imaging method which uses microwave wavelength bands that are unaffected by cloud or lack of illumination from the sun. Such sensors are carried on the ERS-1 and ERS-2, RADARSAT, ENVISAT and the recently launched Sentinel satellites. The Sentinel-1 mission employs C-band SAR imaging, and additionally has a high spatial resolution (25 m in the Extra-Wide swath mode) without compromising the temporal resolution (6-day repeat, but often up to daily coverage) (Torres et al. 2012). This imagery therefore gives the potential to significantly increase the supraglacial lake database during summer, and extend it into the winter. Varying penetration depths of SAR sensors have even allowed the detection of supraglacial lakes covered by ice or snow, or buried at shallow depths (Koenig et al. 2015). Studies utilising SAR techniques for supraglacial lake examinations are limited, however, with only 3 known to date (Johansson & Brown 2012; Joughin et al. 2013; Luckman et al. 2014), and none exploring the newly released Sentinel SAR imagery.

The aim of this project is to use Sentinel-1 imagery, in combination with Landsat-8 imagery, to elicit the spatial and temporal extent of supraglacial lakes on the western GrIS for an extended melt season (June-November). The focus will be on developing an algorithm to

detect supraglacial lakes from the Sentinel images in the summer, but also to extend this into the early winter months due to the availability of SAR imagery compared to optical imagery, which cannot image in darkness. The study site is in southwest Greenland, centred around Jakobshavn Isbræ, due to the high presence of supraglacial lakes and hydrological activity compared to the rest of the ice sheet (Lewis & Smith 2009; Selmes et al. 2011), and preliminary investigations showing the presence of lakes year-round. The main objectives are to:

1. Develop a water-classifying method applicable to summer Sentinel-1 SAR imagery;
2. Explore the potential of the Sentinel imagery to detect supraglacial lake dynamics;
3. Extend supraglacial lake analysis into the early winter.

The first two objectives will involve a comparison with Landsat-8 imagery, in order to assess the suitability and accuracy of Sentinel scenes to depict supraglacial lakes and detect rapid lake drainages. The lake detection will be carried out using semi-automatic methods, although significant manual input will be required, while lake drainages will be pinpointed using a fully-automated algorithm. The final objective will be carried out manually, in order to ensure accuracy as there will be no contemporaneous Landsat images with which to compare or validate results.

2. Literature Review

2.1 – Hydrology of the Greenland Ice Sheet

2.1.1 – The Hydrological System

Below the snowline of the GrIS is an active hydrological system which spans the ice surface (supraglacial system), within the ice (englacial system), beneath the ice (subglacial system) and beyond the ice (proglacial system). Liquid meltwater present on the ice sheet at the highest elevations forms slush zones, but can also channelize into supraglacial streams which flow over the ice sheet (Chu 2014). In the ablation zone, meltwater can pool to form supraglacial lakes in depressions on the ice surface that form as a translation of the bed topography below (Echelmeyer et al. 1991; Lampkin & Vanderberg 2011). This results in lakes being fixed with respect to the bedrock framework, reforming in the same place each year as the amount of meltwater increases (Sneed & Hamilton 2007). The base of an unfrozen lake has a much lower albedo, and thus more than double the ablation rate of the surrounding ice, which contributes to the downward growth and increased depth and volume of supraglacial lakes over the melt season (Lüthje et al. 2006; Tedesco & Steiner 2011; Tedesco et al. 2012).

Supraglacial channels can also form on the downslope side of supraglacial lakes, if the latter fill to breaching-point and overflow (Catania et al. 2008; Selmes et al. 2013). These channels may transport water across the surface to the ice sheet edge, where it is classed as runoff and contributes directly to the mass loss of the GrIS. Alternatively, supraglacial streams may be intersected by a crevasse, a fracture formed by tensile stresses, or a moulin, a near-vertical conduit that links directly to the englacial or subglacial system (Chu 2014). Colgan et al. (2011b) suggest that moulin-type drainage is much more efficient in transporting meltwater pulses (for example diurnal melt fluctuations) than crevasse-type drainage; likely due to differences in penetration depth. Crevasses only form to a depth dependent on the toughness of the glacier ice and, if present, the rate of input of a source of water; if this rate is too slow, the water will refreeze before the crack penetrates deeper. Therefore, a large amount of

water is required to fracture the full ice thickness to connect to the subglacial system (van der Veen 2007; Krawczynski et al. 2009). Conversely, moulins are thought to be semi-permanent features, creating well-connected meltwater drainage pathways that remain active for several years (Catania & Neumann 2010). Crevasses and moulins are thus more likely to feed englacial conduits, which connect the supraglacial system to the subglacial drainage network (Chu 2014). Englacial conduits can also be formed by the incision of a supraglacial channel base due to melting; when the channel reaches a certain depth, the ice above closes by ice deformation, forming a closed tunnel (Fountain & Walder 1998).

Subglacial water transport, by contrast, is affected by the basal conditions beneath the ice such as the presence/absence of basal sediment, the basal roughness and the flux of water. The subglacial drainage system may form a slow-flowing, hydraulically inefficient, distributed system of linked cavities, where water flows through narrow orifices into small cavities between bedrock obstacles (Kamb 1987). This may resemble many small, braided canals that have been eroded into sediment below, as recent modelling efforts have shown a large proportion of the GrIS may be underlain by soft sediment (Bougamont et al. 2014). Alternatively, more hydrologically efficient tunnel systems can form, either eroded downwards into basal sediment, or upwards into the ice (Fountain & Walder 1998; Banwell et al. 2013; Bougamont et al. 2014). If a sustained water input allows the basal water pressure to exceed the ice-overburden pressure, larger tunnels grow preferentially to form an arborescent network, usually culminating in a small number of channels emerging at the margin (Hock & Hooke 1993; Fountain & Walder 1998; Chu 2014). Hydrological models of the GrIS encompass both distributed and channelized flow; as meltwater volumes increase over the ablation season, more channels open, and later close as the supply of water is insufficient to sustain them (Hewitt 2011; Colgan et al. 2011a).

Water can also be stored both englacially and subglacially; Colgan et al. (2011b) found the average residence time of water within the GrIS was 2.2 years. Rennermalm et al. (2013) established that up to 54% of annual ice sheet runoff was stored, likely within englacial or subglacial cavities, until a thaw event triggered its release. Additionally, subglacial lakes have

recently been detected using airborne radar beneath the GrIS (Palmer et al. 2013a), with subsequent theoretical modelling predicting ~1600 potential subglacial lake locations beneath the entire ice sheet (Livingstone et al. 2013). This is similar to observations in Antarctica, where lakes were first detected in 1970 and are now known to occur extensively beneath the ice sheet (Robin et al. 1970; Siegert et al. 2005). Furthermore, subglacial lake drainages have been detected beneath the GrIS (Howat et al. 2015; Palmer et al. 2015), similar to the situation beneath the Antarctic Ice Sheet (Wingham et al. 2006; Fricker et al. 2007). GrIS supraglacial and subglacial lakes may exist in tandem as manifestations of the same bed topography undulations (Sergienko 2013), however the subglacial lakes may contain up to an order of magnitude more water than supraglacial lakes (Palmer et al. 2015).

Meltwater is also stored in supraglacial lakes, if, instead of overflowing and draining, they freeze over at the end of the melt season (Selmes et al. 2013). When lakes melt only around the lake perimeter during summer, features known as ogives form as imprints on the remaining ice cover as the peripheral ice reforms and is advected downglacier with the ice flowing across the stationary supraglacial lake basin. The result is a pattern of bands, with the furthest downstream being the oldest; as one is formed each year, these have been used to calculate ice velocity (Echelmeyer et al. 1991; Darnell et al. 2013). Alternatively, supraglacial lakes can also terminate by rapid drainage through hydraulically-driven fracture propagation; as has already been discussed, an abundant amount of water must pond in order for a water-filled crevasse to propagate through the entire ice thickness to the bed (van der Veen 2007; Krawczynski et al. 2009). Supraglacial lakes can provide such a volume of meltwater, and have been observed to drain rapidly through the ice when a fracture forms in the lake basin, transporting the full lake volume (and subsequent surface melt after drainage) through the ice via a moulin formed within the fracture (Das et al. 2008). Both the sudden and the slower overflow drainage mechanisms of supraglacial lakes can provide substantial pulses of water to the englacial and subglacial hydrological networks above the usual ablation season meltwater transport (Banwell et al. 2013); and as such, have important implications for ice dynamics.

2.1.2 – Impact of Hydrology on Ice Motion

If meltwater reaches the subglacial system, it can have a significant impact on ice dynamics. Zwally et al. (2002) observed the near coincidence of the onset of surface melt in summer and widespread ice acceleration, proposing that meltwater is delivered to the bed where it overwhelms the inefficient distributed hydraulic system. The consequent increase in basal water pressure and decrease in friction between the ice and the bedrock allows for enhanced basal sliding, and thus ice velocity to increase; with a positive correlation between the amount of meltwater and the magnitude of ice acceleration. Furthermore, at the end of the melt season there is a rapid deceleration, which has been attributed to a sudden increase in basal friction and drop in basal sliding once the meltwater supply ceases. Zwally et al. (2002) recorded velocities to drop to 10% below the winter average, taking several weeks to recover to expected winter values. Such a pattern has also been observed by other studies over land-terminating sectors of west Greenland (Joughin et al. 2008), with Palmer et al. (2011) detecting summer velocities up to 48% above the average winter speed, 100 km from the margin. Furthermore, recent modelling has shown that delivery of seasonal meltwater to the bed may weaken subglacial sediment beneath the ice, facilitating the increased velocities; with greater melt production predicted as temperatures increase, even greater velocity amplifications could be expected (Bougamont et al. 2014).

However, other studies have suggested that increasing surface meltwater could alternatively result in stabilised, or declining annual velocities, as short-term enhanced ice velocities are offset by more efficient subglacial water transport (van de Wal et al. 2008; Sundal et al. 2011; Podrasky et al. 2012). Observations near the margins of the GrIS have likened the probable events to those that occur within alpine glaciers on a seasonal basis (Shepherd et al. 2009; Bartholomew et al. 2010; Hoffman et al. 2011). The seasonal evolution of alpine glacier subglacial hydrology with a sufficient supply of meltwater is now well established: an inefficient linked-cavity network present over winter is overwhelmed in early spring with the onset of surface melt. Basal water pressure increases and friction decreases, resulting in local uplift of the ice, greater basal sliding and enhanced ice velocities, a scenario known as “hydraulic jacking”. Over time, however, the cavities and orifices grow by thermal erosion,

and larger conduits grow at the expense of smaller ones. These conduits facilitate much more efficient transport of the meltwater flux, allowing basal water pressure to decrease as water is evacuated through the system at a greater rate, resulting in a frictional increase and reduction in ice velocities. The increased efficiency of the system progresses upglacier with time, often in line with the retreating snowline (Hock & Hooke 1993; Hubbard & Nienow 1997; Nienow et al. 1998; Fountain & Walder 1998).

This seasonal evolution of drainage system efficiency has also been proposed for the GrIS (Schoof 2010), with GPS measurements detecting this switch up to 35 km from the margin (Sole et al. 2011), dye-tracing experiments up to 41 km (Cowton et al. 2013; Chandler et al. 2013), and hydrological observations up to 50 km (Bartholomew et al. 2011). Similar to alpine glaciers, studies have found that increased efficiency occurs at progressively higher elevations (Bartholomew et al. 2010), but is limited by meltwater availability and thus not all basins will transition (Moon et al. 2014). The acceleration that does occur immediately prior to the switch is spatially variable, with greater speeds associated with thicker ice (Tedstone et al. 2014). However, observations have shown that with longer and warmer seasons, the net annual velocity trend will be negative, as the mounting summer velocities in response to melt are mediated by significantly reduced winter speeds (Sole et al. 2013; Tedstone et al. 2013). Borehole studies have postulated that late-summer velocity diminutions are due to the integration of unchannelized areas of the subglacial system becoming increasingly incorporated (rather than further efficiency enhancement of channelized regions) (Andrews et al. 2014). Therefore, the 12% decrease in annual velocities between 2007-2014 recorded by Tedstone et al. (2015), despite a 50% increase in surface meltwater production, could be explained by an annual increase in drainage efficiency of less-connected areas surrounding meltwater channels. Greater volumes of meltwater production associated with warmer summers may continue to be mediated by further inclusion and an earlier switch to a more efficient subglacial hydrological network, thus continuing the trend of declining annual velocities below the equilibrium line (Mayaud et al. 2014; Van de Wal et al. 2015).

Beyond the equilibrium line, conversely, such a decrease in annual velocities has not been observed; instead, annually escalating speeds have been measured up to 140 km from the margin (Doyle et al. 2014). Towards the ice sheet interior, slopes are less steep than at the margins, limiting conduit growth by allowing heat to dissipate as melt rates cannot overcome the greater ice-overburden pressures associated with thicker ice (Meierbachtol et al. 2013; Dow et al. 2014). For conduits to remain open, a sustained water supply is required to produce pressures over the ice-overburden (Dow et al. 2014), and current volumes of surface meltwater production are therefore insufficient to allow a more efficient drainage network to be established (Doyle et al. 2014). The situation at higher elevations on the GrIS may be more akin to that proposed by Zwally et al. (2002), where increased surface melt will enhance subglacial water pressure, basal sliding and thus ice velocities (Mayaud et al. 2014).

2.1.3 – Supraglacial Lakes and Ice Motion

Supraglacial lake drainages can provide an additional water flux to that already transported through the subglacial hydraulic system during the melt season, and thus may further impact ice dynamics. Krawczynski et al. (2009) calculated that 98% of supraglacial lakes in western Greenland contain a sufficient water volume to drive hydrofractures in their basins through 1.5 km of ice. The delivery of such volumes to the ice sheet base through rapid drainage has been suggested to explain late summer velocity variations by overwhelming the subglacial system, even after it has evolved into a more hydrologically efficient system (Bartholomew et al. 2008; Bartholomew et al. 2010). Therefore, hydrological forcing of ice velocity from supraglacial lake drainage can occur whenever the meltwater supply is greater than the capacity of the basal hydraulic network (Cowton et al. 2013; Morriss et al. 2013; Joughin et al. 2013; Mayaud et al. 2014; Bougamont et al. 2014). Even slower-draining supraglacial lakes have been observed to transport a surplus water flux sufficient to locally increase ice velocity: Tedesco et al. (2013) measured a four-fold speedup from such a drainage, compared to a fifteen-fold speedup from a nearby rapid lake drainage. Single lake drainages tend to force ice velocities for short durations, while multiple coincident drainages may contribute to

seasonal dynamics, such as a net summer speedup (countering the increasing efficiency of the subglacial system) (Das et al. 2008; Morriss et al. 2013).

Supraglacial lakes may be of further significance as they form and drain at higher elevations with increasing surface temperatures (Liang et al. 2012; Howat et al. 2013; Morriss et al. 2013; Fitzpatrick et al. 2014). Not only can the volume of water transported during drainage overwhelm an already-efficient subglacial network, but it may be fundamental in both opening new conduits higher on the GrIS (Danielson & Sharp 2013) and forcing the evolution of less efficient systems (Sole et al. 2011). Consequently, further into the ice sheet, where the large ice thickness and minimal presence of meltwater limit the development of channelised drainage, large pulses of meltwater from supraglacial lake drainages may also be significant controls of ice dynamics (Bartholomew et al. 2012; Doyle et al. 2014). At present, drainages have only been observed to contribute to the increasing velocities and seasonal fluctuations in basal sliding at higher elevations, as compared to channelisation closer to the GrIS margins (Doyle et al. 2014; Stevens et al. 2015). However, models based on the latest Intergovernmental Panel on Climate Change (IPCC) future climate warming scenarios have shown that supraglacial lakes may spread over 100 km further inland by 2060, which could eventually provide enough meltwater to the bed where drainage is inefficient to overcome the ice-overburden and force an evolution in efficiency (Leeson et al. 2015). As surface gradients are considerably less steep within the GrIS interior, Bartholomew et al. (2010) state that even a small further temperature increase will induce melt over a substantial area of the ice sheet; greater supraglacial lake extent has already been observed and seems likely to continue. Therefore, the conclusion of the latest IPCC Report that surface meltwater “does not seem to be driving significant changes in basal lubrication that impact on ice sheet flow” (Vaughan et al. 2013, p.357) has been proven invalid by almost all subsequent work. Surface meltwater, and particularly the drainage of supraglacial lakes, is influencing GrIS velocities and studies of the latter are thus of vital importance.

2.3 – Remote Sensing of Supraglacial Lakes

Studies of supraglacial lakes have included *in situ* investigations such as borehole water-level, velocity measurements and supraglacial and proglacial studies (e.g. Das et al. 2008; Tedesco et al. 2013; Doyle et al. 2014; Stevens et al. 2015), observations using time-lapse photogrammetry (Danielson & Sharp 2013), modelling of growth and drainage (e.g. Leeson et al. 2012; Banwell et al. 2012; Arnold et al. 2014), and various remote sensing techniques. Many studies include several, if not all, of these approaches. This review will focus on the latter category, particularly on how lakes are detected within satellite imagery.

2.3.1 – Optical Imagery

MODIS imagery has been widely used to investigate supraglacial lakes due to its very high temporal resolution, with several passes of the GrIS a day. Most studies utilise bandmath combinations of visible wavelengths for lake detection (e.g. Box & Ski 2007), though alternative methods such as fuzzy logic membership functions, thermal bands and average or dynamic reflectance thresholds have also been used (Sundal et al. 2009; Hall et al. 2009; Selmes et al. 2011). MODIS lake detections are often semi- to fully-automated, due to the vast amount of available data, and have been used to calculate area, depth, volume, presence and seasonal evolution of supraglacial lakes over one or multiple years, as well as validating predictions from models (Lüthje et al. 2006; Box & Ski 2007; Selmes et al. 2011; Liang et al. 2012; Leeson et al. 2013; Fitzpatrick et al. 2014). Specific classifications have also been developed that can detect ice-covered lakes, or those present in regions of cryoconite, which are usually difficult to detect with optical imagery (Johansson et al. 2013; Johansson & Brown 2013). However, the 250 m spatial resolution of MODIS puts a lower limit on the size of lake that can be detected: most studies exclude any smaller than 0.125 km² (2 pixels) (Selmes et al. 2011; Liang et al. 2012), though others supplement the dataset with higher resolution imagery, such as Landsat or the Advanced Spaceborne Thermal Emission and Reflection Radiometer (ASTER) (Sundal et al. 2009; Fitzpatrick et al. 2014).

Landsat imagery has a higher spatial resolution than MODIS, allowing more detailed investigations of spatial change, however the temporally-coarse resolution of 16 days limits the extent to which changes can be pinpointed in time (Morriss et al. 2013). Landsat-focused studies tend to depict water with the Normalised Difference Water Index (NDWI), which utilises ratios of the red and blue bands, or further modifications of the NDWI (for example, near-infrared and green bands have been incorporated) due to the varying reflectances of water and ice at different wavelengths (Huggel et al. 2002; Xu 2006; McMillan et al. 2007; Gardelle et al. 2011; Morriss et al. 2013; Banwell et al. 2014; Fitzpatrick et al. 2014; Pope et al. 2016). Other studies manually delimit lake boundaries (introducing a degree of subjectivity) (Lampkin 2011; Lampkin & Vanderberg 2011; Hoffman et al. 2011), utilise textural analysis (Lettang et al. 2013) or determine a threshold value from the histogram of normalised image pixel values (Morriss et al. 2013; Howat et al. 2013). Only one paper to date has used the Landsat-8 Operational Land Imager (OLI), launched in 1993 with a superior spatial resolution (30 m) compared to previous Landsat satellites, to investigate supraglacial lakes (Pope et al. 2016).

Alternative optical imagery used for supraglacial lake detection has included ASTER, with a 15 m resolution but lower spatial coverage (Sneed & Hamilton 2007; Georgiou et al. 2009), and WorldView imagery, with an even higher resolution of 2 metres (Yang & Smith 2013; Smith et al. 2015). However, WorldView consequently has a much smaller spatial coverage (17 km swath width compared to 2330 km for MODIS), and is expensive to obtain (Pope et al. 2016). Furthermore, the usefulness of optical imagery is severely limited by cloud cover, which can result in a significant number of images having to be discarded. Sensors can only image in hours of daylight (i.e. summer months), but are additionally affected by specific illumination conditions which change with the solar zenith angle (Georgiou et al. 2009). Therefore, although optical sensors have many advantages for investigating supraglacial lakes, their capabilities have practical limitations.

2.3.2 – Radar imagery

Radar (RADio Detection And Ranging) imagery can go some way to improving the limitations of optical imagery; as sensors provide their own signals (unlike optical imagery), they can operate in any light condition, so are unaffected by lack of illumination by the sun. These signals also penetrate clouds, so can image in nearly any meteorological conditions (Van Zyl & Kim 2011). However, application of real aperture radar systems for supraglacial lake investigation has been relatively limited. Jezek et al. (1994) employed a surface-based radar to investigate firn melt zones in western Greenland, while Hall et al. (2009) used the Quick Scatterometer in combination with MODIS to study surface and sub-surface melt. Buried subglacial lakes were detected using the Operation IceBridge Snow Radar (Koenig et al. 2015), however other glaciological applications of radars have included subglacial lake detection (Palmer et al. 2013b), bed topography mapping (Gogineni et al. 2014) and subsequent ice thickness measurements (Enderlin et al. 2014).

Synthetic Aperture Radar (SAR) systems, conversely, have been much more extensively used for glaciological applications. SAR is a sidelooking system that uses the movement of the satellite to generate a greater aperture without an extremely long antenna, allowing images to be taken at a higher resolution than real aperture radars (sub-metre to a few tens of metres) (Van Zyl & Kim 2011). SAR sensors have been used to investigate sea ice dynamics (Smith 1996; Nghiem & Bertoia 2001; Nakamura et al. 2006; Partington et al. 2010), measure ice thickness and map bed topography (Legarsky et al. 2001; Xiaoqing et al. 2013; Wang et al. 2015), pinpoint glacier termini (Moon & Joughin 2008), and determine surface velocities through feature tracking (Luckman & Murray 2005; Pritchard et al. 2005; Tedstone et al. 2014), speckle tracking (Joughin et al. 2010; Howat et al. 2011; Joughin et al. 2014) or intensity tracking between images (Sundal et al. 2011). SAR systems also offer the potential to track ice velocity through interferometry, which acquires additional information from images of the same scene taken from various vantage points. Several contemporaneous images allow determination of surface topography, while separation of these images by a given time allows a map of surface velocities to be produced (Van Zyl & Kim 2011). Many studies have utilised the interferometric capabilities of SAR to calculate velocities over a section, or all of the GrIS

(Joughin et al. 1995, 1996, 2004, 2008, 2013; Rignot et al. 1995, 2011; Bamber et al. 2000; Rignot & Kanagaratnam 2006; Moon et al. 2014).

Hydrological investigations of the GrIS using SAR have been less numerous, but hold great potential due to the ability to overcome the limitations of optical and real aperture radar systems. Such studies include large-scale topographic surveys of the ice sheet surface (Rott & Mätzler 1987; Vornberger & Bindschadler 1992; Bindschadler & Vornberger 1992), interpretations of the varying reflections of different melt, firn or slush zones (Fahnestock et al. 1993; Jezek et al. 1993, 1994; Jezek 1999; König et al. 2001), measurements of penetration depths of different radar frequencies (Rignot et al. 2001), or calculations of the number of melt days by measuring the wetness of the ice surface (Holt et al. 2014). Lakes in permafrost environments have been successfully mapped using SAR, including calculations of depth and ice thickness (Nolan et al. 2002; Duguay & Lafleur 2003; Brown & Young 2006; Hirose et al. 2008), however, only three studies known to date have investigated supraglacial lakes using SAR. Joughin et al. (2013) used TerraSAR-X images simply to pinpoint the time of lake drainage, while Luckman et al. (2014) employed ENVISAT Advanced SAR (ASAR) to investigate backscatter from lakes on the Larsen C Ice Shelf in Antarctica. Johansson & Brown (2012) manually mapped supraglacial lakes on the western GrIS, also using ENVISAT ASAR, but during winter in order to avoid issues with the similar reflection of water in the slush zone to lakes. Although experiencing some success in mapping lakes, they suggest that SAR imagery should only be a supplement, rather than replacement for optical imagery, due to its inability to detect small or narrow lakes, and those in complex topography.

2.3.3 – Sentinel-1

The conclusions of Johansson & Brown (2012) regarding the usefulness of ENVISAT ASAR imagery to detect supraglacial lakes are likely a consequence of the low spatial (150 m) resolution. The Sentinel-1 mission, conversely, offers freely-available imagery with a superior

resolution of 25 m in the Extra-Wide swath mode, specifically aimed at collecting polar imagery, with a temporal resolution of only 6 days due to the two-satellite constellation, compared to 35 days for ENVISAT ASAR (Torres et al. 2012; Malenovský et al. 2012; Wegmüller et al. 2015). Due to the very recent launch (imagery available from October 2014), applications of Sentinel-1 imagery are limited. Ardhuin et al. (2015) detected sea ice wave heights, Muckenhuber et al. (2016) investigated sea ice drift, and Nagler et al. (2015) have used the Interferometric-Wide swath mode to produce an ice sheet wide velocity map for the GrIS. Furthermore, the Sentinel SAR uses dual polarisation, which has only recently been incorporated into SAR satellites (e.g. RADARSAT-2) and holds much greater potential for ice-related studies as the backscatter responses are affected by differing environmental variables (Scheuchl et al. 2004; Partington et al. 2010; Nagler et al. 2015; Muckenhuber et al. 2016).

3. Methodology

3.1 – Study Site

The study site is a ~42,000 km² region of southwest Greenland, centred around Jakobshavn Isbræ, reaching as far north as Lille Gletscher and south past Inuppaat Quuat (Figure 1). This region is significantly larger than many previous supraglacial lake studies, aside from the ice-sheet-wide investigation of Selmes et al. (2011); the margin length of just their southwest region was 1331 km, compared to ~450 km in this study. Jakobshavn Isbræ is the largest GrIS outlet glacier, draining ~7.5% of the total GrIS (Joughin et al. 2004; Luckman & Murray 2005; Nick et al. 2013). Since 1995, observations have shown the marine-terminating glacier to be thinning, accelerating and retreating (Thomas et al. 2003) which was initially triggered by warm oceanic waters reaching the terminus (Holland et al. 2008) and subsequent collapse of the ice tongue (Joughin et al. 2010). More recent velocity increases of the glacier, however, have been explained by increased presence of meltwater-filled crevasses, weakening the ice (van der Veen 2007; Colgan et al. 2011b). Podrasky et al. (2012) suggest that velocity is

positively correlated with meltwater input on diurnal timescales, and negatively on intra-seasonal timescales. Meltwater presence on Jakobshavn Isbræ therefore impacts upon the ice dynamics of the glacier.

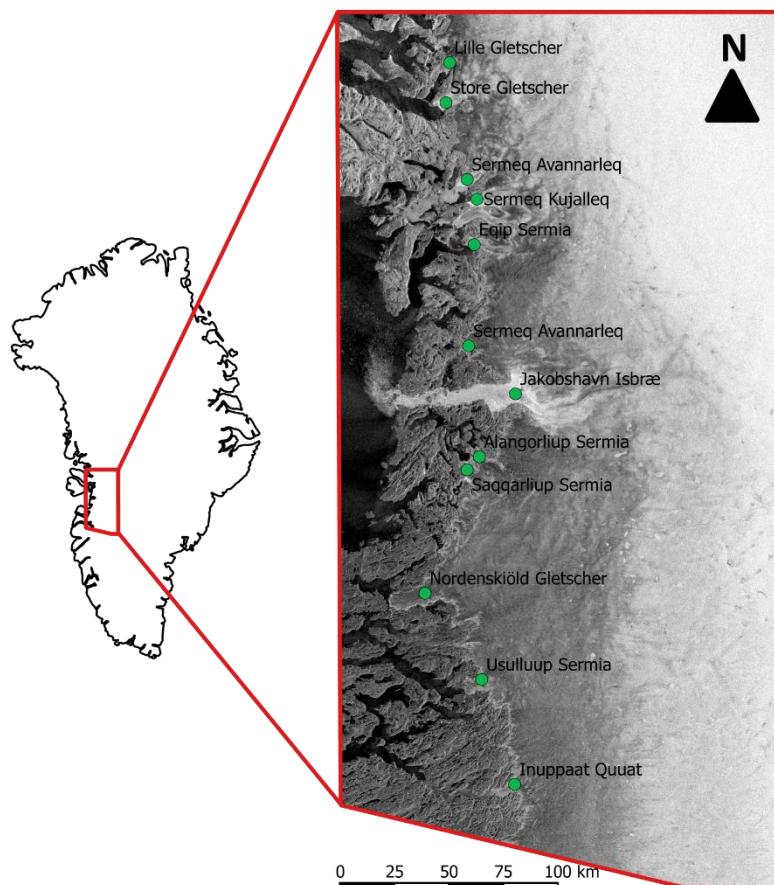


Figure 1 - Location of the study site within Greenland. The inset shows the main drainage catchments mapped on a Sentinel image from DoY 287, HH polarisation

Southwest Greenland is known to have a high prevalence of surface meltwater and meltwater dynamics; for example, Selmes et al. (2011) found this region contained 55% of all GrIS supraglacial lakes, and 61% of all rapid lake drainage events. Many studies have focused particularly around Jakobshavn Isbræ (Box & Ski 2007; Georgiou et al. 2009; Selmes et al. 2011; Lampkin 2011; Lampkin & Vanderberg 2011; Liang et al. 2012; Howat et al. 2013; Pope et al. 2016); thus a large number of results are available to validate findings of this study employing previously unused Sentinel imagery. The specific study area was chosen by the total extent of selected Landsat-8 scenes, as carried out by Pope et al. (2016); the same number of paths were used (006, 007, 008, 009, 010) but fewer rows than their study (011, 012), resulting in the current study area extending less far south. Not all of the Landsat and Sentinel images covered the full study area extent, however all possible scenes were included in order to obtain the best temporal resolution possible. The percentage coverage of each image of the full study region is shown in Table 1 for the Landsat imagery, and Table 2 for the Sentinel imagery.

3.2 – Methods

3.2.1 – Lake Detection

The flow chart in Figure 2 displays the processing used from the acquisition of the raw imagery to the creation of a binary lake mask. Landsat and Sentinel scenes over the chosen study area (Fig.1) were acquired from the USGS Earth Explorer and ESA Sentinel Hub websites respectively for dates between mid-June and September 2015 for summer lake and drainage detection, and additional Sentinel images from October to November 2015 were downloaded for extension into early winter months (USGS 2016; Copernicus 2016). Atmospherically corrected Landsat-8 OLI Surface Reflectance images with less than 10% cloud cover were downloaded (Table 1; Fig.2A), and the only pre-processing required was re-projecting certain scenes to Universal Transverse Mercator (UTM) 22N, mosaicking concurrent scenes imaged on the same day, and cropping out the bedrock and ocean within QGIS using a mask created from the Greenland Ice Mapping Project (GIMP) Digital Elevation Model (DEM) (Howat et al. 2014).

Table 1 - Landsat-8 OLI images used in the summer lake detections and drainage analysis

Image Acquisition (Day of Year (DoY))	Resolution (m)	Number of Scenes	Percentage Coverage of Full Study Area	Used for Drainage Analysis
171	30	1	24%	Y
178	30	1	5%	Y
180	30	2	83%	Y
187	30	2	62%	Y
189	30	2	66%	Y
196	30	2	86%	Y
198	30	1	27%	Y
210	30	1	28%	Y
212	30	2	86%	N
214	30	1	26%	Y
228	30	1	39%	Y
235	30	1	46%	Y
237	30	1	55%	Y

Table 2 - Sentinel images used in the summer lake detections and drainage analysis

Image Acquisition Date (DoY)	Resolution (m)	Number of Scenes	Percentage Coverage of Full Study Area	Used for Drainage Analysis
166	40	1	83%	N
167	40	1	52%	N
176	40	1	41%	N
177	40	2	60%	N
184	40	2	100%	Y
188	40	1	41%	Y
189	40	2	60%	Y
190	40	1	89%	Y
191	40	2	100%	Y
196	40	1	40%	N
200	25	1	41%	Y
201	40	2	60%	Y
208	25	2	100%	Y
212	25	1	11%	N
213	25	2	60%	Y
220	25	2	100%	Y
224	25	2	41%	Y
225	25	2	41%	Y
232	25	1	55%	Y
237	25	2	60%	Y
239	25	1	100%	Y
244	25	2	100%	Y
249	25	2	60%	Y
256	25	2	100%	Y
261	25	2	60%	Y
263	25	1	100%	Y
268	25	2	100%	Y
273	25	2	60%	Y

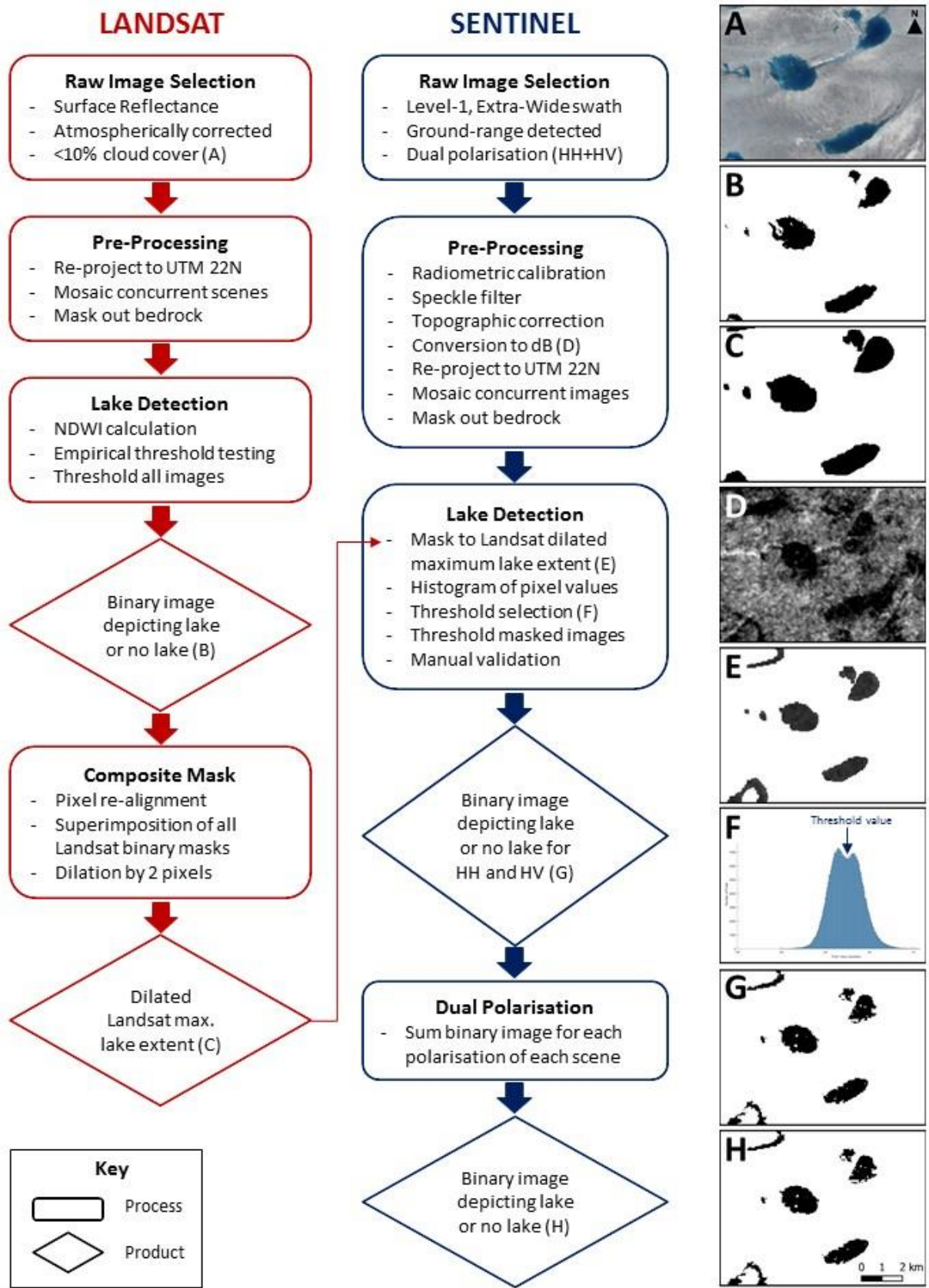


Figure 2 - An illustrated flow diagram outlining the methodology followed for both the Landsat and the Sentinel lake detections. A) shows example lakes from a Landsat false colour RGB image on DoY 189, and D) shows these lakes in the pre-processed HH-polarised Sentinel image on DoY 189

The Sentinel scenes alternatively required significantly more pre-processing. SAR Level-1 images (C-band, 5.4 GHz) were chosen as most appropriate due to being georeferenced but minimally processed. The Extra-Wide swath (400 km with 5 sub-swaths) provided the best coverage without comprising the spatial resolution, for which the highest possible was chosen (Medium Resolution of 40 m for the first part of the summer; High Resolution of 25 m for the remainder; Table 2). Dual polarisation images (HH+HV) were chosen in the Ground-Range Detected mode, which uses multiple looks in order to reduce speckle, although this is at the expense of a slightly reduced spatial resolution (ESA 2016). The total number of Landsat scenes obtained was 13, while the Sentinel summer images numbered 28.

The raw Sentinel scenes were then pre-processed within the Sentinel Application Platform (SNAP) toolbox. This involved a Radiometric Calibration, to ensure pixel values can be directly related to the radar backscatter, a Single Product Speckle Filter, which improves image quality by removing speckle texturing caused by random interference of the return waves, and a Topographical Correction (Copernicus 2016). The last process was carried out using a Range Doppler Terrain Correction Operator, which corrected the terrain and image orientation using bilinear interpolation of the GETASSE30 DEM, outputting a georeferenced file in the UTM 22N projection. The GETASSE30 DEM is of significantly lower resolution than the images prior to terrain correction. Although this step reduces the resolution from several metres to those stated in Table 2, it is currently the best option within the SNAP toolbox. The images were loaded into QGIS and the backscatter values converted to decibels using the equation:

$$Image (dB) = 10 \times \log(image)$$

From this point, the two polarisations (HH and HV) of each image were treated as separate images, rather than a single scene with two bands. Concurrent images were mosaicked, and the bedrock cropped out using the same mask as for the Landsat scenes (Fig.2D). For some of the Sentinel scenes acquired on the same day, pre-processing resulted in a non-contiguous boundary between the two edges being stitched together; the resultant space of less than a pixel between the two images was treated as 'no data' values, and taken into account in subsequent processing.

The pre-processed images were then used to detect supraglacial lakes. For the Landsat imagery this was calculated using the NDWI, a well-established bandmath method of the ratio of the red (band 4, 0.64-0.67 μm) to blue bands (band 2, 0.45-0.51 μm) (Pope et al. 2016):

$$NDWI = \frac{B_2 - B_4}{B_2 + B_4}$$

Other bandmath combinations were investigated, including Near-Infrared (NIR) to-blue and green-over-NIR (Gardelle et al. 2011), green-to-NIR (Chen et al. 2013), red-to-NIR (Morriss et al. 2013), blue-to-NIR and coastal-to-NIR (Jawak & Luis 2014). Visual comparison proved that the NDWI was the most accurate at depicting supraglacial lake extents, and further justified by Pope et al. (2016) who also used the red and blue bands of Landsat-8 scenes to define supraglacial lake extent. Two thresholds were then chosen empirically from the resultant images, a lower value of 0.2 to encompass all water and a higher value of 0.5 to include only lakes, and applied to all the scenes in order to produce a binary image where 1 indicates water, and 0 ice (Fig.2B). The images masked with the higher threshold were re-projected in order that all pixels aligned, and were superimposed using the Mosaic tool in ArcGIS in order to create a composite mask of the maximum lake area defined by the Landsat imagery.

A similar method was attempted for the Sentinel images, whereby a direct threshold was selected from the histogram of pixel values of each image. However, this proved to be extremely erroneous, despite lakes being clearly visible in most scenes (e.g. Fig.2D). Therefore, the composite Landsat lake mask was dilated by 2 pixels (60 m, chosen empirically by application to several images; Fig.2C) and applied to each Sentinel scene as a mask, producing an image showing the Sentinel backscatter values within each maximum lake area as defined by the Landsat thresholding, and a 2-pixel buffer of ice around each lake (Fig.2E). Such a method, followed by an edge detection algorithm, was used by Yang & Smith (2013) to depict supraglacial streams in WorldView imagery. The edge detection technique was tested for the Sentinel imagery using Canny and Sobel edge detectors in MATLAB, but was also entirely unsuccessful in defining lakes. Instead, the histogram of each masked image was plotted, and, if a bimodal distribution existed between the lower lake values and higher ice values, the lowest point between these peaks was selected as a threshold for that particular

image (Fig.2F). Significantly, the histograms of the images cropped by the dilated Landsat composite mask were completely different compared to those of the original, unmasked scenes. A similar technique was used by Liang et al. (2012) and Howat et al. (2013) to select a threshold value according to the tail distribution of histograms. The Sentinel images cropped to the Landsat maximum lake extent were then thresholded by their unique value in order to mask out non-water areas and produce a binary image akin to the thresholded Landsat images (Fig.2G).

This method proved to be successful in delineating lakes with reasonable accuracy. Due to the incorporation of the Landsat imagery in the method, validation of the Sentinel lake extents against the Landsat could not be justified. Therefore, the thresholds were adjusted with reference to the original Sentinel image, and discarded if no clear bimodal histogram distribution was present to allow a threshold to be selected. This left a total of 22 Sentinel images through the summer, still significantly greater than the Landsat total of 12.

The final stage in the lake detection involved summing the binary images of the two polarisations for each day (Fig.2H). Figure 3 shows the lake area detected by each polarisation for each Sentinel scene, clearly showing that in the majority of cases the HV polarisation picks up much larger lake areas. The lake areas depicted by each polarisation often differed; therefore, by combining the two binary images, a more accurate representation of lake area could be obtained. For the three days that a simultaneous Landsat and Sentinel image were available (DoY 189, 212 and 237), a comparison of the total lake areas detected by each polarisation, both polarisations, and the Landsat thresholding was carried out for the overlapping area of the Landsat and Sentinel images. A further comparison was also made on an individual lake basis for 20 lake areas within these intersecting areas. The areas of the 20 lakes calculated from each image were then used to calculate both the root mean square error (RMSE) and the RMSE per km² (RMSE/km²) which display the error in the classified lake area and the error per 1 km² lake respectively (Sundal et al. 2009; Selmes et al. 2011; Liang et al. 2012; Pope et al. 2016):

$$RMSE_{Sentinel} = \sqrt{\frac{\sum((A_{Sentinel} - A_{Landsat})^2)}{n}}$$

$$RMSE/km^2_{Sentinel} = \sqrt{\frac{\sum((A_{Sentinel} - A_{Landsat})^2)}{\sum(A_{Sentinel})}}$$

where A refers to lake area (km^2) and n the total number of lakes summed within the numerator. Individual lake areas calculated from the Landsat were plotted against the respective lake areas determined from the Sentinel imagery; and the difference in the Landsat and Sentinel lake areas were calculated ($Area_{Sentinel} - Area_{Landsat}$) and plotted against the mean elevation for each lake, obtained from the GIMP DEM (Howat et al. 2014).

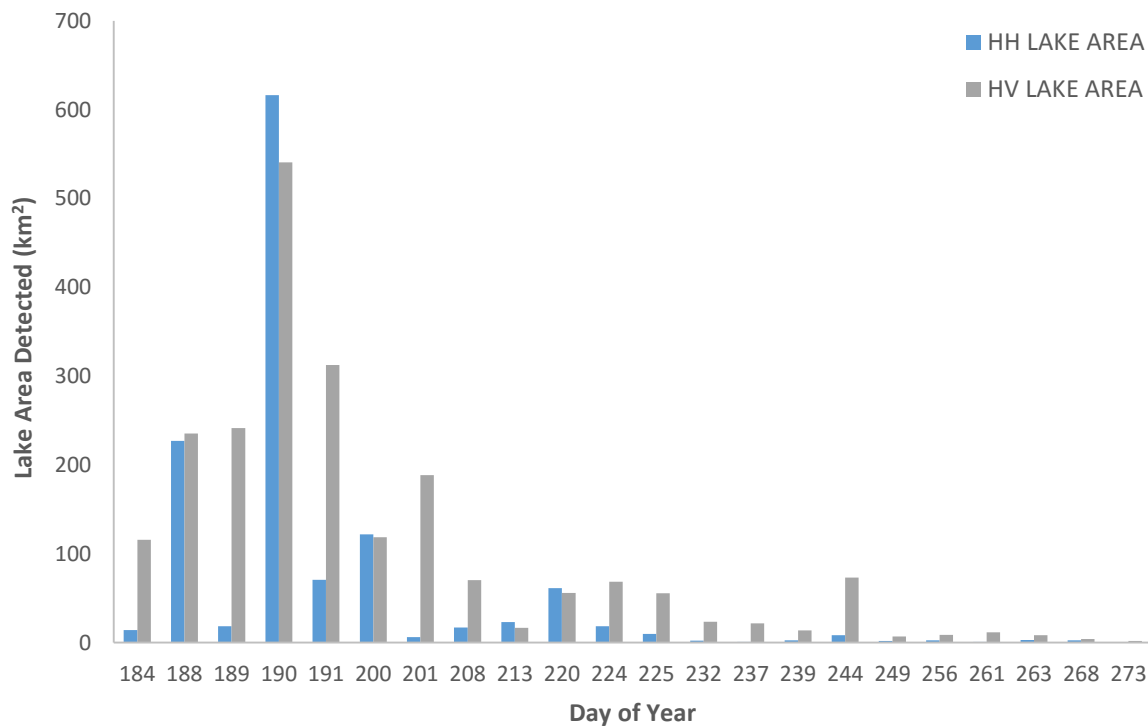


Figure 3 - Lake area detected on each day by the HH and the HV Sentinel polarisations

Finally, the total lake area calculated by each method over the summer months was calculated. As both the Landsat and the Sentinel images covered varying proportions of the total study site (Tables 1 and 2), it was necessary to standardise the lake areas in order to

compare them. This was calculated by multiplying the lake area from each image by the proportion of the total study area that that image covered.

3.2.2 – Lake Drainage

Once lake extents for all 12 Landsat and all 22 Sentinel images were produced, rapid drainage events were detected using an algorithm scripted in MATLAB. Lake drainages are often easily distinguished within the Sentinel imagery, as shown in Figure 4: if the darker areas of lower backscatter created by the lakes suddenly produce higher backscatter values similar to the surrounding ice (Fig.4D-F, yellow circles), this is interpreted as a lake drainage. An intermediate stage has also been observed, where the low backscatter from the lake flips to very high backscatter values for several days, before then producing lower values similar to the surrounding ice (Fig.4D-F, red and green circles). This sequence is interpreted to be the result of a thin water layer left behind after the initial drainage, producing the high backscatter values, before also draining. This sequence was also noted by Johansson & Brown (2012) using ENVISAT ASAR. However, the brighter lake basin does not always occur post-drainage, thus could not be used to pinpoint all drainages. The drainage detection script creates a maximum lake extent array from all summer lake extents, then tracks each individual lake area within its maximum extent from each image to the next. The algorithm was run twice, once for the Landsat imagery, and once for the Sentinel, in order to compare the outputs. Any scenes that did not cover the full study area were extended to the full extent, with these additional areas designated 'no data' values. Rapid drainage events were defined as a lake losing at least 80% of its area within 96 hours, for lakes greater than 25 pixels (0.0225 km²). The temporal period of four days was chosen with regard to the average time between each Landsat and Sentinel image, and fits well within the literature: Fitzpatrick et al. (2014) also defined a rapid drainage as occurring within four days, while Liang et al. (2012) chose a period of five days and Selmes et al. (2011) two days. The lake size of 0.0225 km² is smaller than that often used by MODIS (0.125 km² due to the coarser spatial resolution (Selmes et al. 2011)), and was defined by manual inspection of the smallest draining lakes. The 'day of

drainage’ was defined as the mid-point of the two images between which the lake disappears (Doyle et al. 2013), with an associated positive and negative error of half the number of days between these images.

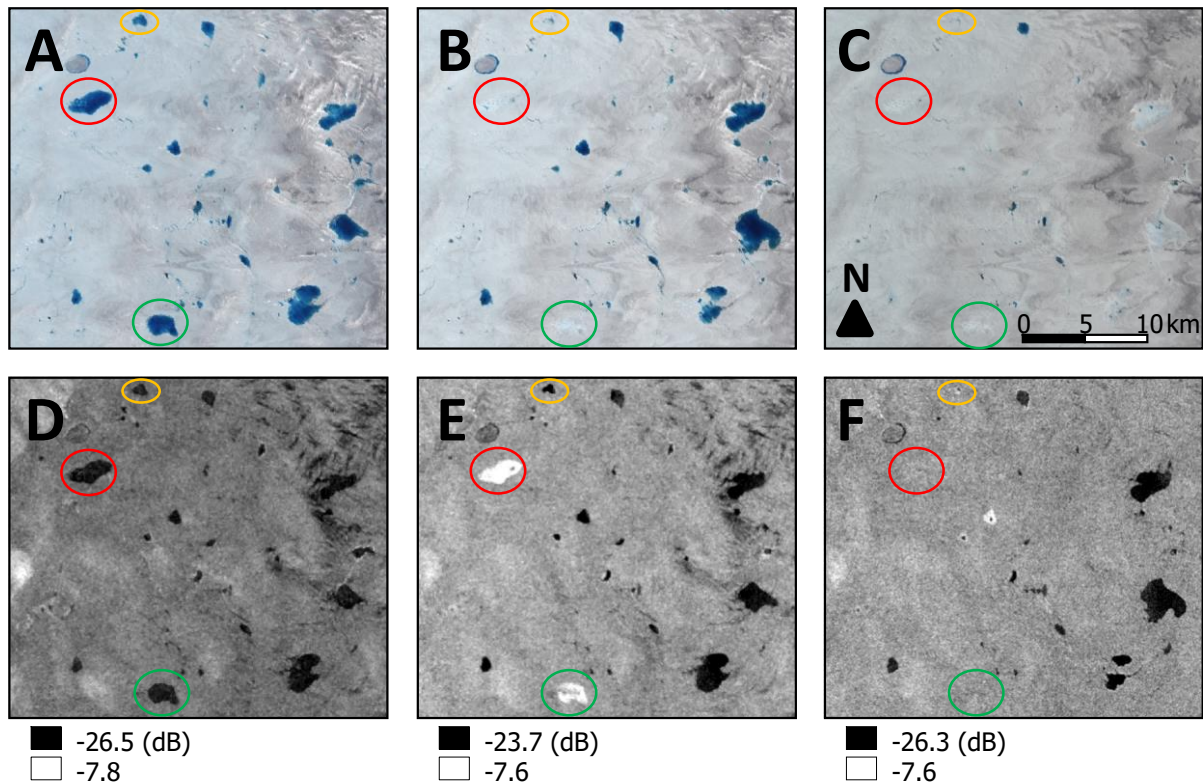


Figure 4 - Example rapid lake drainages in the Landsat imagery (A-C) and Sentinel imagery (D-F). Image A) was acquired on DoY 189, B) on DoY 196, C) on DoY 212, D) on DoY 188, E) on DoY 190, and F) on DoY 200

The algorithm detected an enormous number of events for both the Landsat and the Sentinel runs; manual validation of actual drainage events was carried out using the respective original images. Scenes that only covered a subsection of the full study area were a particular issue, as if any ‘no data’ values were present within a lake basin (for example where two Sentinel images were mosaicked together but the boundary was not contiguous), the script marked this as a lake drainage. All drainages therefore had to be checked with subsequent imagery to determine whether the lake disappearing was a drainage or a misidentification due to no data values. Alternatively, there were also misidentifications as a result of the lake detection method in Section 3.2.1; there were some days where the Sentinel or the Landsat lake classification did not accurately depict a lake area on one day, resulting in a drainage event

being depicted despite the lake being present in the subsequent image. Due to the large number of results, only lakes over 0.2 km² were validated as this size is predicted to be the lower limit that could cause drainage by hydrofracture (Krawczynski et al. 2009). The number of drainages to be validated subsequently decreased from thousands to hundreds. However, future work would be able to account for erroneous drainages due to no data values, reducing the amount of manual validation required and allowing investigation of smaller lake drainages detected in Sentinel imagery that would not be possible from MODIS scenes.

3.2.3 – Lake Freeze-Over

The behaviour of supraglacial lakes at the end of the melt season was also investigated in both the Landsat and Sentinel imagery. The Sentinel scenes are significantly more useful in detecting freeze-over of lakes due to the greater number of images and availability later in the year once there is insufficient sunlight for optical sensors to image, but also due to the ability of the SAR sensor to image through clouds and snow. Snowfall affected the Landsat images from mid-August (DoY 228) onwards, obscuring the majority of lakes, however, areas of darker backscatter were still clearly visible in the Sentinel images, suggesting that liquid water was present beneath this snow cover (Fig.5). The lakes in the Sentinel from the time of snowfall onwards produce a slightly higher backscatter than earlier in the year; this is interpreted as the shallow snow cover contributing to the backscatter, whilst also suppressing some of the lower backscatter from the liquid water beneath. Previous studies investigating lake freeze-over with optical imagery defined freezing as being related to sub-zero surface temperatures or a lack of surface melting (Selmes et al. 2013; Johansson et al. 2013; Luckman et al. 2014). However, SAR allows a direct detection of the point of freeze-over: bubbles entrained within lake ice as it freezes increase the relative backscatter (Hirose et al. 2008). Therefore, the backscatter signal of unfrozen and frozen lakes is distinct enough to allow identification of freeze-over (as carried out by Johansson & Brown (2012) using ENVISAT ASAR), which was defined as having occurred once values within the lake basin were comparable to that of the surrounding glacial ice. This was carried out manually within the study region; a total of 300 lakes were detected to freeze-over. The 'day of freeze-over' and

associated positive/negative error was calculated in the same way as the day of lake drainage, and plotted against mean lake elevation and lake size to assess any immediate trends.

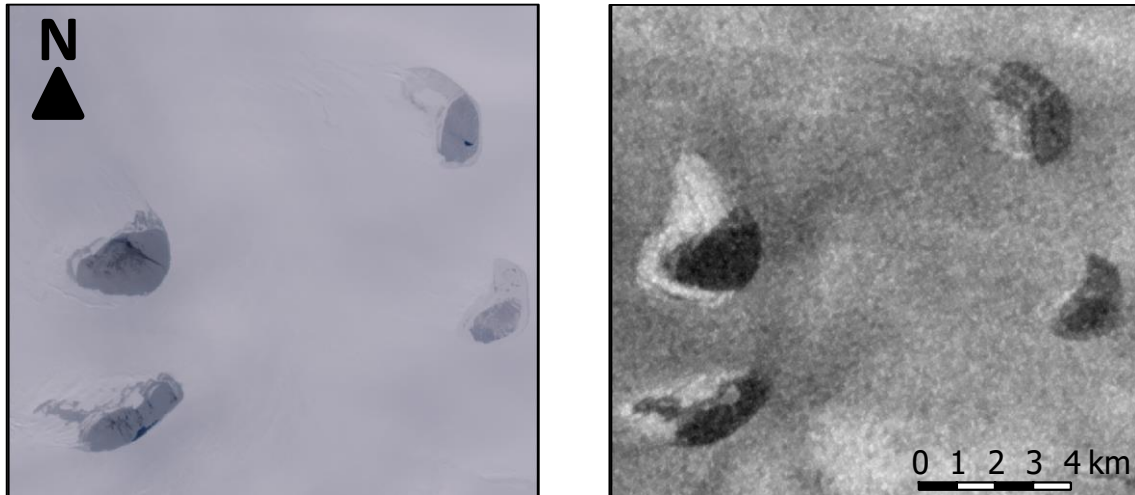


Figure 5 - An example of supraglacial lakes obscured by snow in the Landsat RGB false colour image on DoY 235, but liquid water still visible in Sentinel image (HV polarisation) on DoY 232

3.2.4 – Buried Lakes

The advantages of Sentinel imagery over optical sensors outlined in Section 3.2.3 offers a further avenue for supraglacial lake analyses; i.e. an extension into the early winter. Late in the summer, small dark areas appear in the Sentinel imagery at higher elevations than the supraglacial lakes previously identified (Fig.6). These are either never visible in the Landsat scenes, or appear as large depressions which remain mostly frozen through the summer except for a small amount of melting around their perimeter. The darker Sentinel regions appear beneath this ice cover and have similar backscatter values to the snow-covered unfrozen lakes in Section 3.2.3; therefore, these later appearances are interpreted as ponded liquid water beneath the surface, where the ice and snow cover above provide an insulating layer allowing liquid water to persist later into the year. These features were delineated manually, as there were no contemporaneous Landsat images that would have allowed a similar procedure of lake detection as carried out in Section 3.2.1. A total of 150 features were identified over the study site.

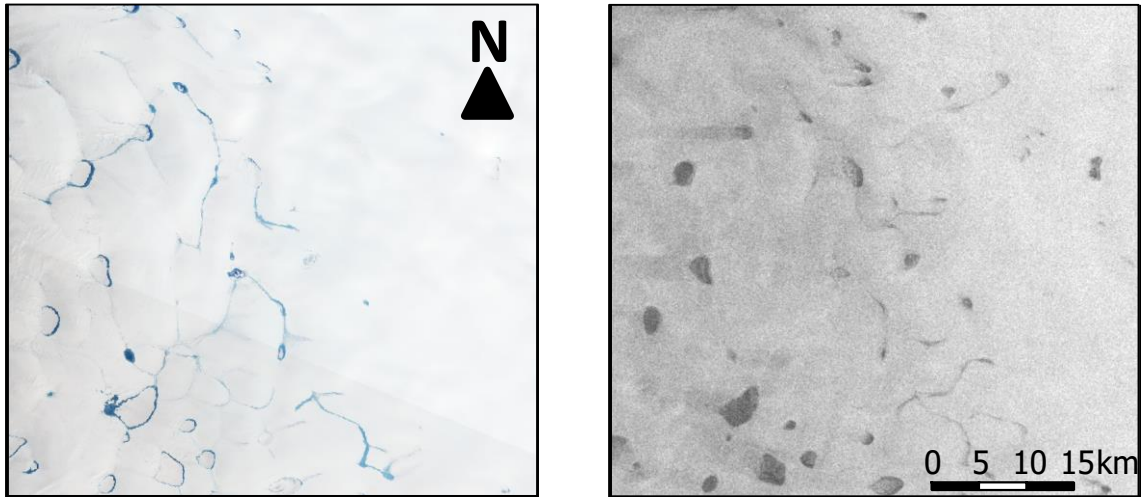


Figure 6 - An example of buried supraglacial lakes that are either partially visible due to melting, or not visible at all in the Landsat false colour image (left; DoY 212), compared to the later Sentinel image (right; acquired DoY 239, HH polarisation) where the full melted extent of these lakes can be seen (a later Landsat scene was not available in this location due to cloud cover)

The formation mechanism of these subsurface lake features will not be considered here; the focus will be on the ability of Sentinel imagery to detect their appearance and disappearance, which would not be possible with optical sensors. However, the lake features mapped in this study show an extremely similar distribution and density of occurrence to the buried lakes mapped by Koenig et al. (2015) using IceBridge Ice Sounding Radar (Fig.7). Considering the

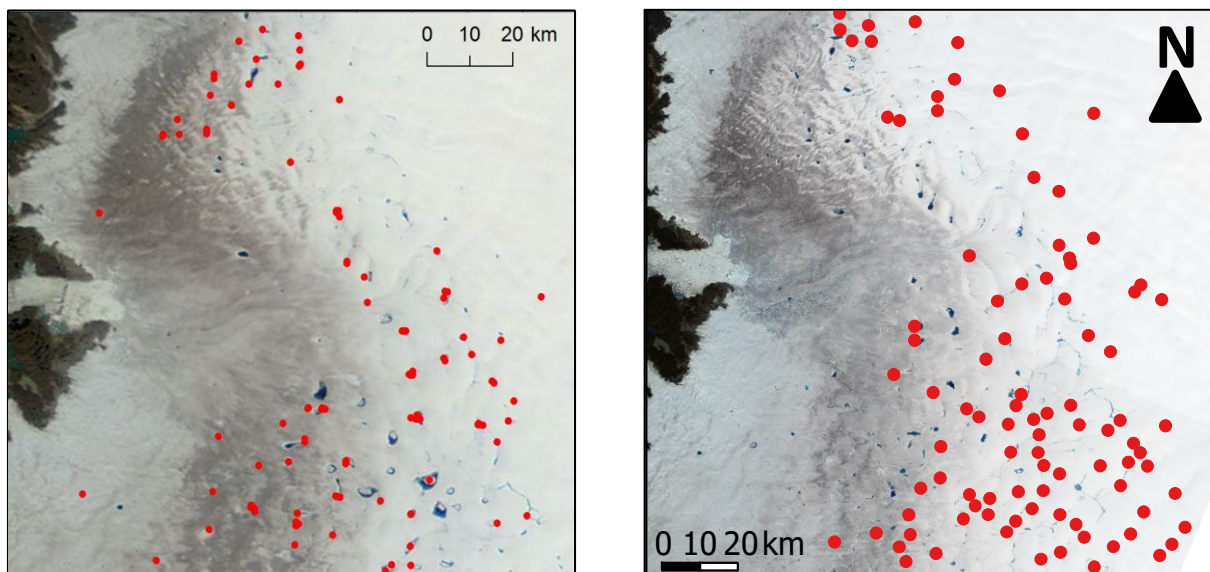


Figure 7 - Comparison of the buried lake distribution mapped by Koenig et al. (2015, Figure 3) using IceBridge Ice Sounding Radar (left), to a section of the buried lakes mapped in the current study over the same extent as the Koenig study (right). The Koenig diagram background is a MODIS image from August 2010; the right is a Landsat false colour from DoY 212 (late July) in 2015

similar distributions, and the subsurface location of the lake features according to the Sentinel imagery, it is interpreted that the lake features may be analogous with the buried lakes identified by Koenig et al. (2015), and will therefore be referred to as buried lakes hereafter. The non-identical situation of some lakes in Figure 7 is not seen as conflicting evidence: Koenig et al. (2015) note that buried lakes usually only appear for a single year; thus as they map the lakes between 2009-2012, the locations in 2015 would not be expected to be identical. The day of appearance and disappearance of each buried lake and associated positive/negative error was determined manually as the midpoint between the two images where the lake first/last occurred, as with the supraglacial lake freeze-over analysis in Section 3.2.3. The size and elevation of each lake was calculated, and plotted against the day of appearance and disappearance respectively.

4. Results

4.1 – Lake Detection

Lake detection using threshold values taken from the bimodal distributions of the masked Sentinel images proved to be a reasonably successful method for depicting lake areas, producing nearly comparative results to the NDWI thresholding of Landsat-8 imagery. Figure 8 shows an example of Landsat and Sentinel lake detections from DoY 189 and DoY 212. The overall detections are similar: the DoY 189 subsection shows the Sentinel to generally depict individual lake areas nearly as well as the Landsat (Fig.8A-C). However, the DoY 212 Sentinel lake detection is less accurate compared to the Landsat (Fig.8D-F). The lakes that are clearly visible in the Landsat false colour image are poorly depicted by the Sentinel thresholding, and additional water is also picked up by the Sentinel that is not present in the Landsat false colour or in the Landsat thresholded NDWI image. Figure 8 is therefore interpreted to show that the Sentinel lake detection can overestimate lakes areas in comparison to the Landsat NDWI classification. This can also be seen in Table 3, which compares the total lake area of the 20 lakes selected from the overlapping areas of the Sentinel and Landsat scenes on each of the three days that an image was available from both sensors. The Sentinel total lake area for all three days is significantly greater than the Landsat total lake area, with the percentage differences between the Sentinel and Landsat varying enormously from 13.3 and 109.7%. However, the RMSE values for the 20 lake areas are not significantly larger than values cited in the literature. DoY 189 shows the greatest RMSE value of 0.34 km², with the other two days producing lower values, while the RMSE/km² values are all very similar (0.14-0.15). For comparison, Selmes et al. (2011) calculate a RMSE of 0.11 km² per lake and RMSE/km² of 0.04, Sundal et al. (2009) obtain a RMSE value of 0.22 km² and RMSE/km² of 0.045, and Liang et al. (2012) obtain values of 0.20 km² and 0.027 respectively.

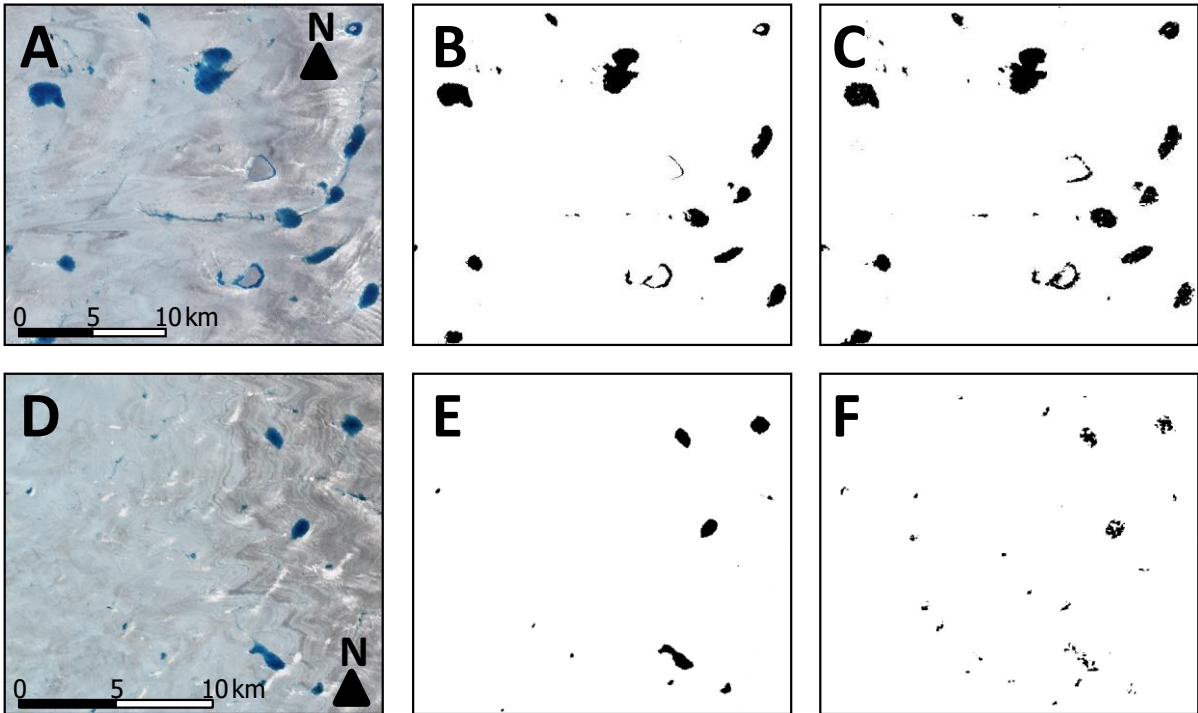


Figure 8 - Examples of the Landsat NDWI lake classifications (B,D) and Sentinel lake detections (C,F) with Landsat RGB false colour images for reference (A,D). The top row shows lake detections for a subsection on DoY 189; the bottom row displays a different region of the study area on DoY 212

Day of Year	Total Image Area (km ²)	HH Sentinel Total Lake Area (km ²)	HV Sentinel Total Lake Area (km ²)	HH + HV Sentinel Total Lake Area (km ²)	Landsat Total Lake Area (km ²)	Percentage Difference between Sentinel and Landsat Areas	RMSE (km ²)	RMSE/ km ²
189	13,1560	6.9	149.7	150.6	110.3	36.6%	0.34	0.14
212	3,255	1.9	5.0	5.0	4.4	13.3%	0.08	0.15
237	9,502	0.1	9.7	9.7	4.6	109.7%	0.09	0.14

Table 3 - Statistics from the Landsat and Sentinel lake detection methods for 20 lakes on each of the three days for which an image was available from both sensors

A further comparison of the individual lake areas depicted by the Sentinel and Landsat methods is shown in Figure 9. The total image and lake area for DoY 189 is significantly greater than the subsequent two dates (Table 3), therefore it is expected that the individual lake sizes are also larger. This is because the image was acquired near the peak of the melt season, whereas DoY 212 and 237 are much later in the season after a number of lakes have drained.

The lake areas calculated by the two methods have a very strong positive linear relationship, with R^2 values for all three dates above 0.91 (Fig.9). To assess any potential bias in lake detection at different elevations, the difference in lake areas between the two methods are plotted against the mean lake elevation in Figure 10. There is no clear trend on any of the three days, as the difference in lake areas varies both with the elevation and between the three days. There is a slight positive trend, implying that the Sentinel imagery depicts greater lake areas than the Landsat methodology. This is clearest above 1200 m elevation (Fig.10), which may suggest that the Sentinel lake thresholding method overestimates lake area more at higher elevations. However, at the highest elevations very little bias exists, and at lower elevations of ~1000 m on DoY 212 the Sentinel method underestimates compared to the Landsat. However, at ~1000 m elevation on DoY 237 there is more of a positive bias. Overall, it appears that elevation is an unlikely explanation for the difference in Landsat and Sentinel lake area detection methods.

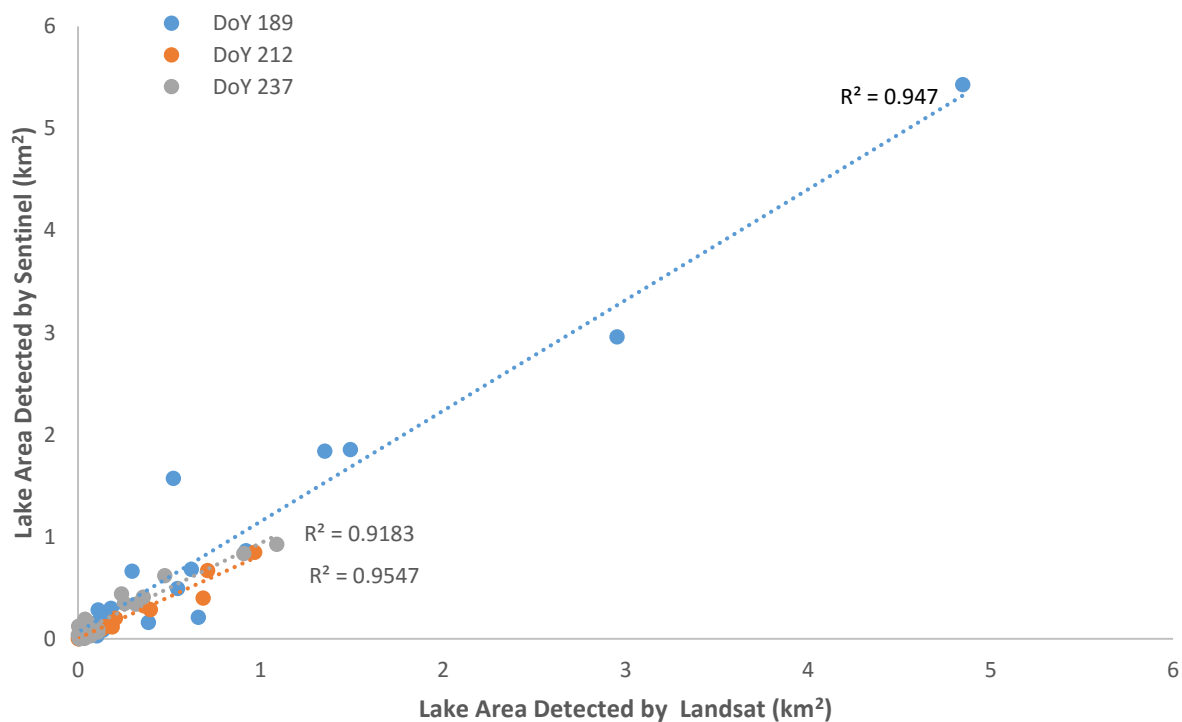


Figure 9 - Graph plotting lake area detected by the Landsat NDWI lake classification against the area for the same lake as detected by the Sentinel method for 20 lakes on each of the three days that an image was available from both sensors

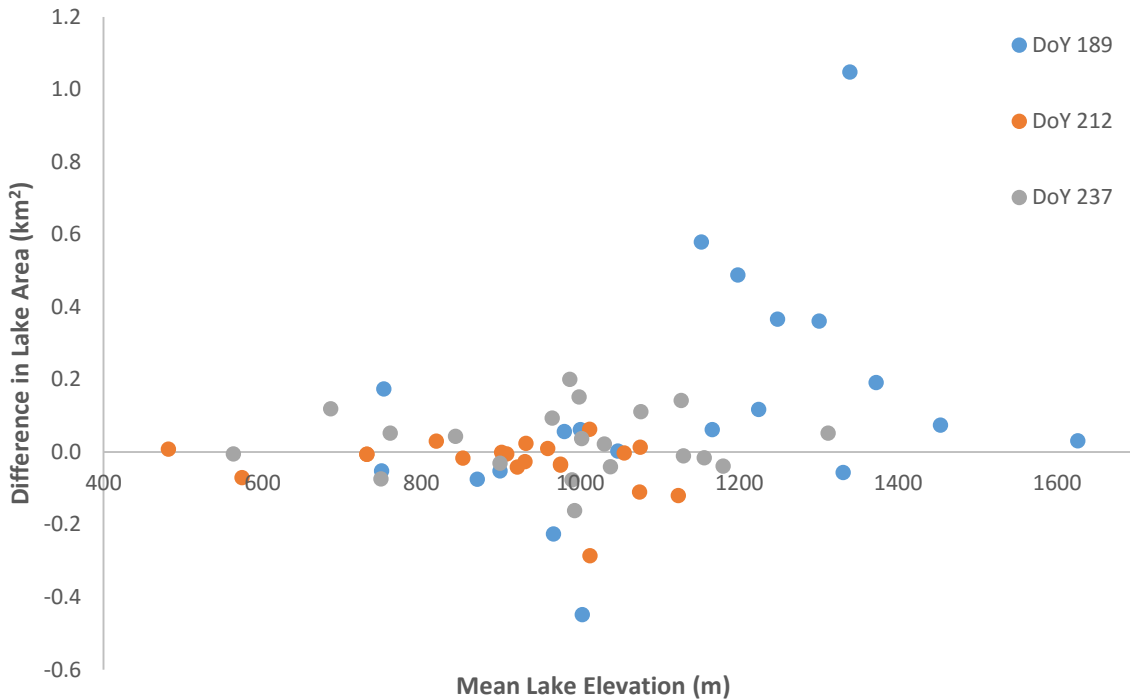


Figure 10 - Difference in the lake area calculated by the Sentinel and Landsat methods for 20 lakes for each of the three days that an image was available from both sensors, plotted against the mean elevation of each lake

Table 3 also shows the contribution of each of the Sentinel polarisations to the calculation of total lake area. The HV polarisation is by far the best at detecting lake area when compared against the area detected by the Landsat technique. While the HH polarisation does detect some water areas, most of these areas are also depicted by the HV polarisation. The lake areas that were detected by either one or both polarisations are shown for each Sentinel image in Figure 11. Although the lake areas for a small number of days were detected by both the HH and the HV polarisations, on most days the lakes were only detected by one polarisation. Figure 3 confirms that it is primarily the HV polarisation that detects these lakes, although there are several days on which the HH polarisation depicts a greater area than the HV polarisation. Thus, the results shown in both Figure 11 and Figure 3 validate the final stage in the Sentinel lake detection methodology of summing the lake detections of the HH and the HV polarisation (Fig.2), as both the polarisations are necessary in order to obtain the best detection of lake area.

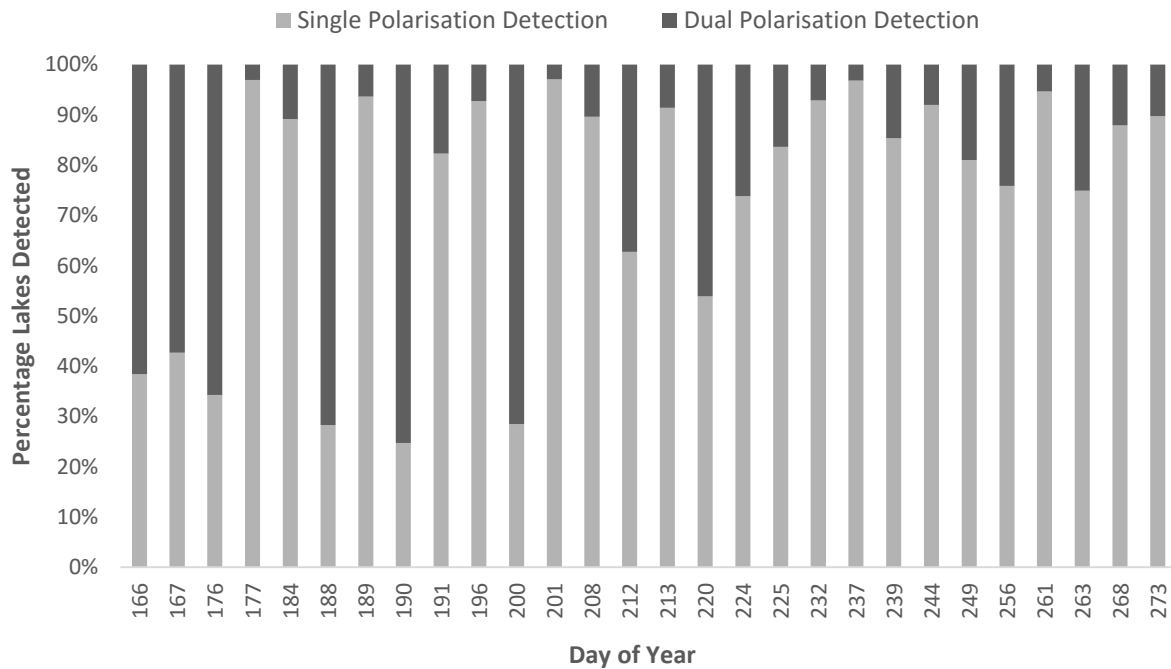


Figure 11 - Graph displaying the proportion of the lake areas detected each day by only one polarisation (either HH or HV), or by both the polarisations

Figure 12 demonstrates two subsections of the study area for each Sentinel polarisation where the lake detection methodology could not accurately depict the lakes areas. The top row of Figure 12 shows several lakes on DoY 201 as they appear in the original Sentinel HH polarised image (Fig.12B) and HV polarised image (Fig.12C), and a Landsat false colour image from the closest day possible (Fig.12A). While the HV polarised image shows the lakes to produce a region of low backscatter, as is expected, the HH polarised image instead show these lakes to have very high backscatter values. The lakes in the HH polarised image would therefore not have been detected by the thresholding of the Sentinel images; this is clearly an error as these lakes are visible in the Landsat and the HV polarisation. The second set of images in Figure 12 (D-F) from DoY 191 show a set of lakes to have disappeared from the HH polarisation, whilst still present in the HV polarisation (circled). On this day, the HV polarisation picks up a significantly greater lake area than the HH polarisation (Fig.3); this situation of lakes temporarily disappearing only in the HH polarisation is the case for nearly half the summer images. Furthermore, at higher elevations in both polarisations on DoY 191 (Fig.12E&F), the topography becomes much more complex and there are more areas of lower backscatter equivalent to the lakes, despite no water being visible in the Landsat false colour

image (Fig.12D). The similar backscatter values of water and this complex topography likely resulted in overestimation of individual lake areas as evidenced in Figure 10.

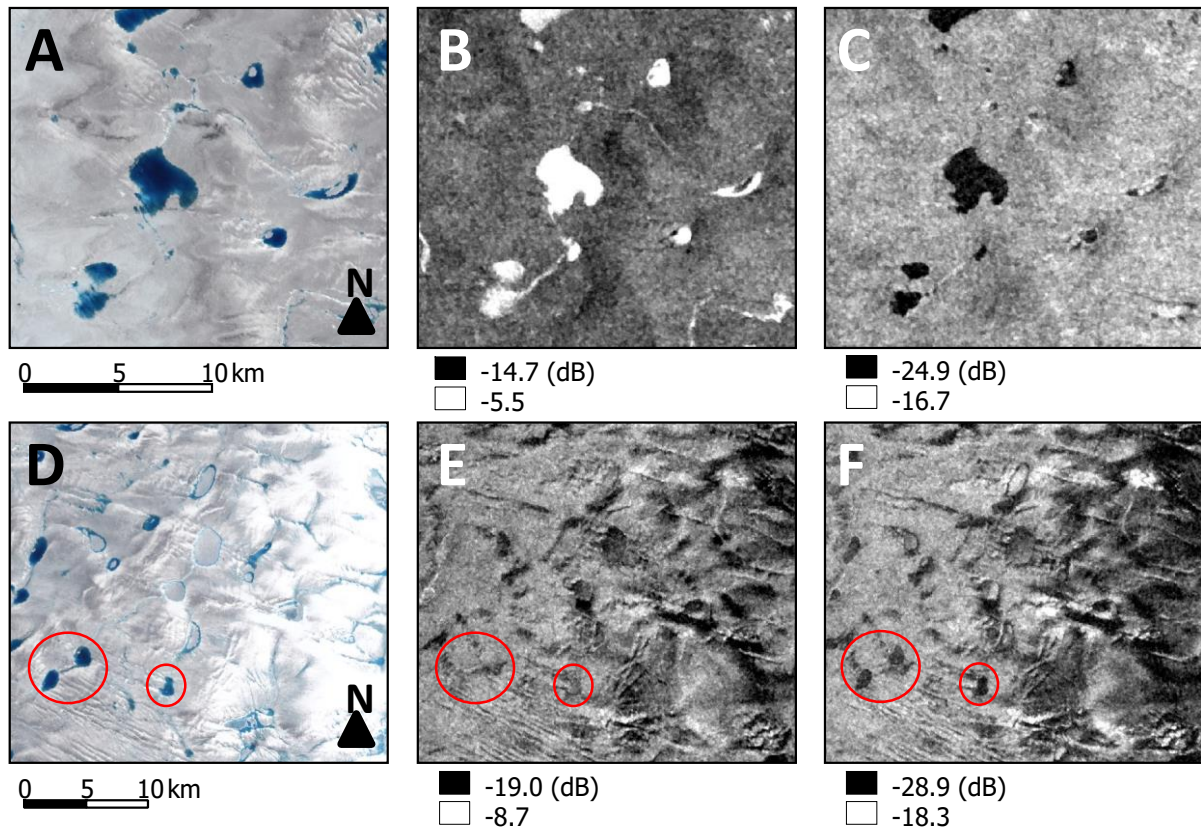


Figure 12 - Example of where the Sentinel lake detection method may not have accurately depicted lakes; the backscatter response of the Sentinel HH polarisations (B,F) are shown with the HV polarisation acquired on the same day (C,F) with a Landsat false colour image on DoY 189 for reference. Subsets B and C were imaged on DoY 201; E and F on DoY 191

As the Sentinel lake detection method was quite successful at determining lake areas when compared to contemporaneous Landsat lake areas detected by the NDWI method (Table 3; Figure 9), the standardised total lake areas calculated by each method will be discussed. It is important to remember that only some of the Sentinel and Landsat scenes covered the entire study area, thus the standardised lake areas shown in Figure 13 have effectively been extrapolated across the full study site and do not represent a totally accurate depiction of the total lake area. A primary observation from Figure 13 is that the total lake areas calculated by the Sentinel on DoY 188 and 190 are outliers and likely to be erroneous, based on both the other Sentinel and the Landsat values. Similarly, the Sentinel value on DoY 244, and Landsat

value on DoY 178 also appear to be erroneous. Manual comparison against the pre-processed Sentinel images for these dates shows that on DoY 188 and 190, large areas of slush at high elevations were incorrectly classified as lakes. Likewise, on DoY 244, large areas of cryoconite were designated as lakes. However, despite these limitations, the trend in total lake area over time for the Sentinel data is similar to that for Landsat, although, as previously mentioned, the Sentinel method mostly overestimates the total lake area compared to the Landsat technique. Disregarding the values on DoY 188 and 190 for the reasons given above, the maximum standardised lake area is 407.6 km² on DoY 189 from the Sentinel, and 355.5 km² on DoY 198 from the Landsat.

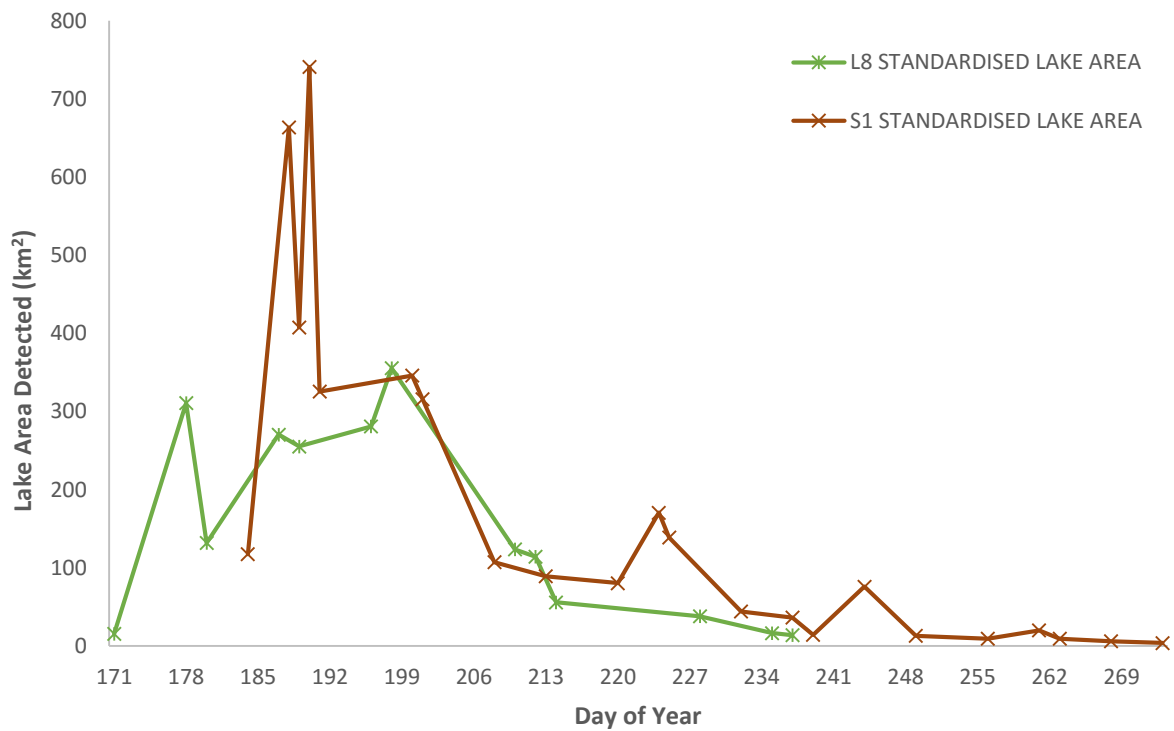


Figure 13 - Graph displaying the total lake area, standardised according to the proportion each image covered of the full study site, against time for the Landsat (L8) lake detections and the Sentinel (S1) lake detections

A further key result is the presence of lakes in the Sentinel images that are beyond the temporal limit of Landsat imagery. This is shown in Figure 13 and Tables 1 and 2, where the useable Landsat imagery ceases in late August (DoY 237). However, the Sentinel lake detection continues to detect lakes through to the end of September, over a month later (DoY

273). Therefore, not only does the Sentinel imagery provide a better temporal resolution than Landsat imagery to assess the lifespan of supraglacial lakes on the GrIS, but has a further benefit of allowing the termination of lakes to be determined, where clouds and darkness prevent optical imagery from obtaining useful scenes.

4.2 – Lake Drainage

The rapid drainage detection algorithm was successful in identifying drainages for both the Landsat and Sentinel lakes. The total number of Landsat drainages was only 4 due to the larger intervals between the Landsat scenes, with 18 additional misidentified drainages due to inaccurate depiction of lake area from the lake detection method, while 50 drainages were detected from the Sentinel imagery, with 52 additional misidentified drainages. Two of the Sentinel drainages were reclassified as freeze-over near the end of the melt season when compared with the Landsat false colour image, leaving a total of 48 drainages. The misidentified drainages quoted above do not include those due to ‘no data’ errors – these numbered an additional 232 events for Landsat and 371 for Sentinel. Therefore, although the script was useful, manual checking was crucial to validate real drainages from the vast number of events that were artefacts. Table 4 displays the mean day of drainage and associated error for the two types of imagery, with the mean lake size and elevation of the drained lakes, however, due to the small number of events no real conclusions can be drawn from these data. The difference in the number of detected drainages does show that the Sentinel imagery is able to detect many more drainages with more precision; the error associated with each drainage date is lower than the error for each date obtained from the Landsat (Table 4). Figure 14 shows examples of the drainage detections using the two types of imagery, with both the day of drainage and associated error mapped for each image set. Due to the Landsat imagery detecting 4 events, only a subsection of the study region is shown for each image set, covering these 4 events. Notably, only two of the four Landsat drainage events are also recorded by the Sentinel method, but very similar dates are obtained for these drainages: the Landsat technique calculates both lakes to drain on $\text{DoY } 188 \pm 1$, while the Sentinel method identifies

the more northern lake to drain on DoY 190.5 ± 0.5 , and the lake to the south to drain on DoY 189 ± 1.5 . Taken together, the southern lake drainage can be pinpointed to have occurred between DoY 189 and 190, while a closer inspection of the northern lake drainage informs that while the majority of the lake drains also drains between DoY 189 and 190, a small but significant lake area remains, and drains between DoY 190 and 191. This second stage of drainage is depicted by the Sentinel lake detections, but not by the Landsat lake detections.

Imagery	Total number of drainage events	Mean day of drainage (Day of Year)	Mean positive and negative error (\pm days)	Mean lake area (km ²)	Mean lake elevation (m)
Landsat	4	185.8	1.0	0.8	1069
Sentinel	48	190.7	0.7	0.6	1052

Table 4 - Statistics from the drainage detections of the Sentinel and the Landsat data

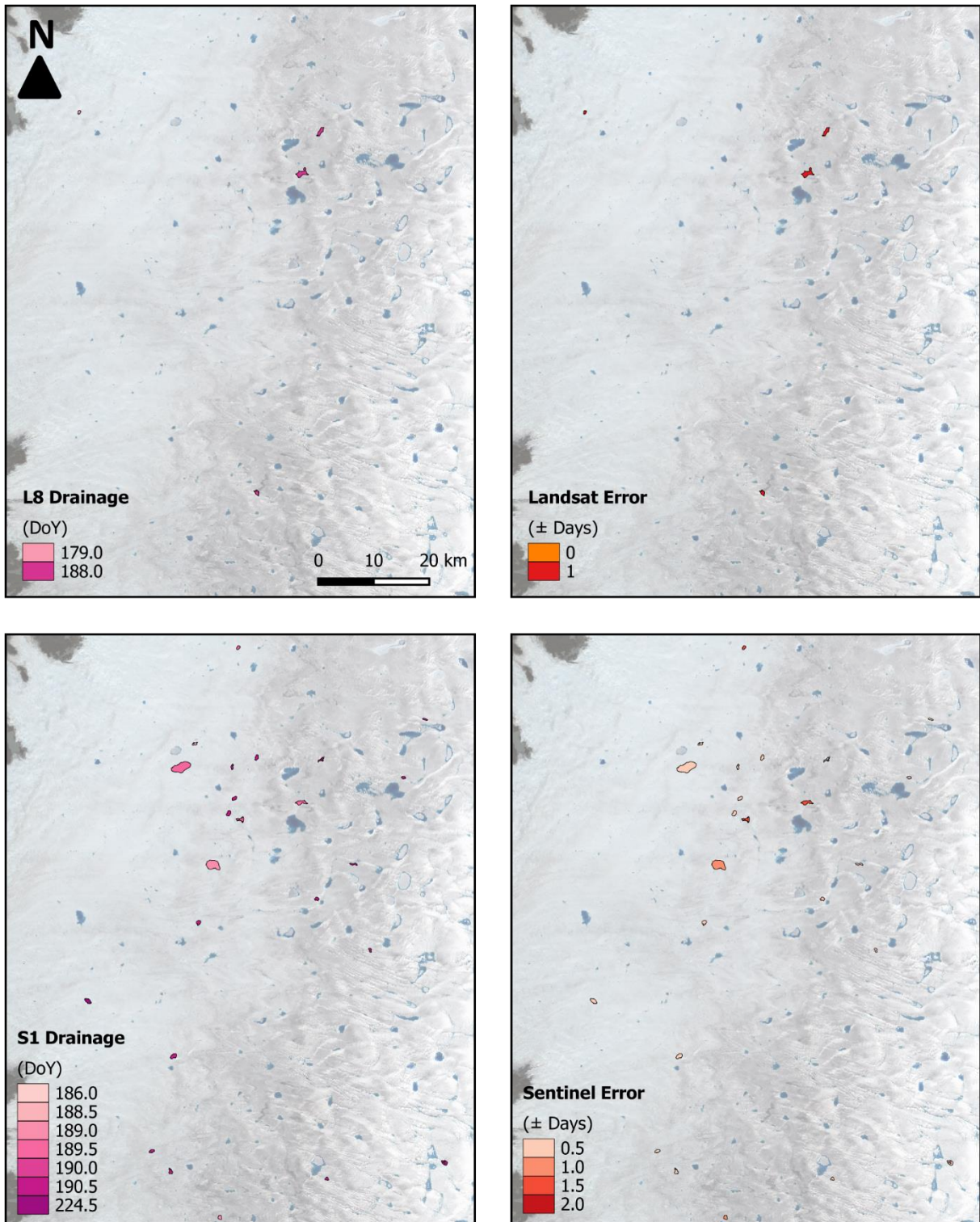


Figure 14 - Example drainage date detections from the Landsat (L8, top row) and the Sentinel (S1, bottom row) data. The day of drainage is mapped for each lake in the left-hand image, and the associated error for that date mapped in the right-hand image. The background image is a Landsat false colour scene acquired on DoY 196

4.3 – Lake Freeze-Over

The results of the manual identification of lake freeze-over from the Landsat and Sentinel images showing the mean day of freeze-over and associated error are mapped in Figure 15 and plotted against the mean lake elevation in Figure 16. These figures both highlight the limited number of Landsat dates compared to the Sentinel, simply due to the number of each image type available. This also affects the errors associated with each drainage date; the error bars in Figure 16 are significantly greater for the Landsat dates than the Sentinel dates. Additionally, the mean error is over twice as long for the Landsat freeze-over dates, with an error of ± 8.3 days compared to only ± 3.7 days for the dates from the Sentinel images (Table 5). The availability of Sentinel imagery well into the winter results in much later freeze-over dates being detected, with the latest freeze-over occurring on DoY 292 compared to DoY 231.5 from the Landsat imagery, and the mean freeze-over date occurring 15.3 days later in the Sentinel imagery compared to the Landsat imagery (Table 5). The snowfall present from DoY 228 onwards has likely had a significant impact on the identification of the day of freeze-over: lakes in the Landsat obscured by snow were assumed to be fully frozen, whereas the Sentinel can penetrate shallow depths of snow and would therefore still record the backscatter from liquid water beneath the snow. The year-round availability of Sentinel imagery, and the ability of its SAR to image through clouds, in darkness, and particularly through shallow snow layers is a key advantage over optical imagery in the analysis of supraglacial lake lifecycles and determination of lake freeze-over dates.

Imagery	Mean day of freeze-over (Day of Year)	Mean positive and negative error (\pm days)	Earliest and latest freeze-over dates (Day of Year)	Mean lake area (min and max) (km ²)	Mean lake elevation (min and max) (m)
Landsat	224.8	8.3	220.0 – 231.5	1.2 (0.03 – 6.9)	1249 (427 – 1712)
Sentinel	240.1	3.7	204.5 – 292.0		

Table 5- Statistics from the freeze-over date detections of the Sentinel and the Landsat data

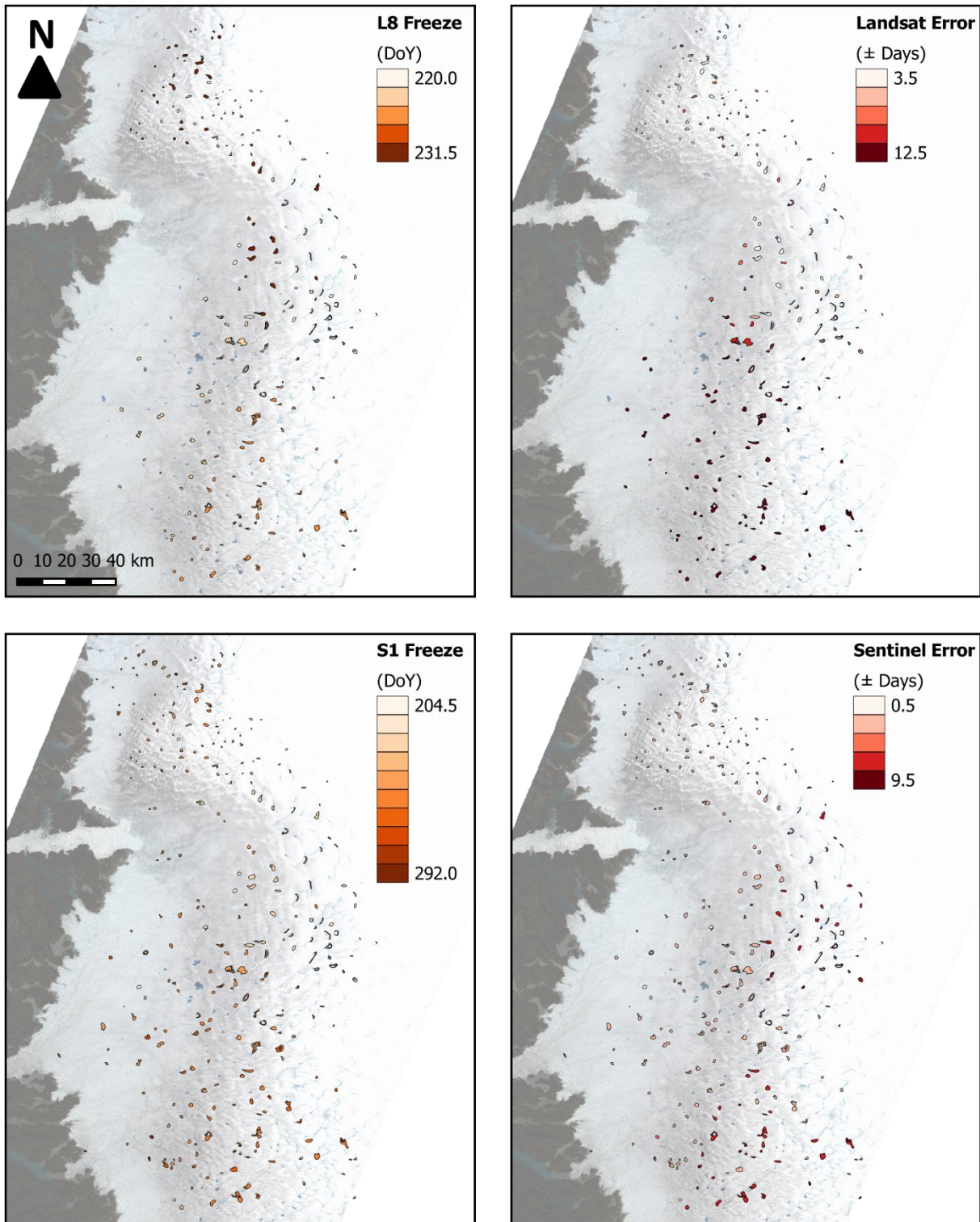


Figure 15 – Supraglacial lake freeze-over date detections from the Landsat (L8, top row) and the Sentinel (S1, bottom row) data. The day of freeze-over is mapped for each lake in the left-hand image, and the associated error for that date mapped in the right-hand image. The background image is a Landsat RGB false colour scene acquired on DoY 196

The pattern of freeze-over dates shown in Figure 15 suggests that the Landsat freeze-over dates show a weak trend with elevation, with lakes at higher elevations freezing earlier and those at lower elevations freezing later. However, approximately 50 km south of Jakobshavn Isbræ, lakes at all elevations apparently freeze on one of two days. This is also apparent from the Sentinel freeze-over dates in Figure 15: there is a general down-glacier trend in lake freeze-over with time and although this trend does not appear to be particularly strong, it is the case that the lakes at the highest elevations freeze first, and those near the ice sheet margin freeze latest. Figure 16 confirms that the relationship between freeze-over dates and elevation are weak, with trend line R^2 values of only 0.10 for Landsat and 0.16 for Sentinel. It is also instructive to compare the mean lake area and elevation of the lakes that freeze-over to those that were detected to drain rapidly (Tables 4 and 5), as the mean size of lakes that freeze over (1.2 km^2) is significantly greater than those that drain (0.6 km^2). However, caution is required when comparing the lake area data: both these values were obtained from the Landsat maximum lake extent mask. This was appropriate for the lake drainage, as lakes tend to drain once they have reached their maximum size during the melt season, however, while this was the case for some lakes that froze, others were significantly smaller by the date of freeze-over. The difference in elevation between lakes that drained and lakes that froze at the end of the melt season is significant; the mean elevation of freezing lakes was $\sim 200 \text{ m}$ greater than the mean elevation of lakes that drained.

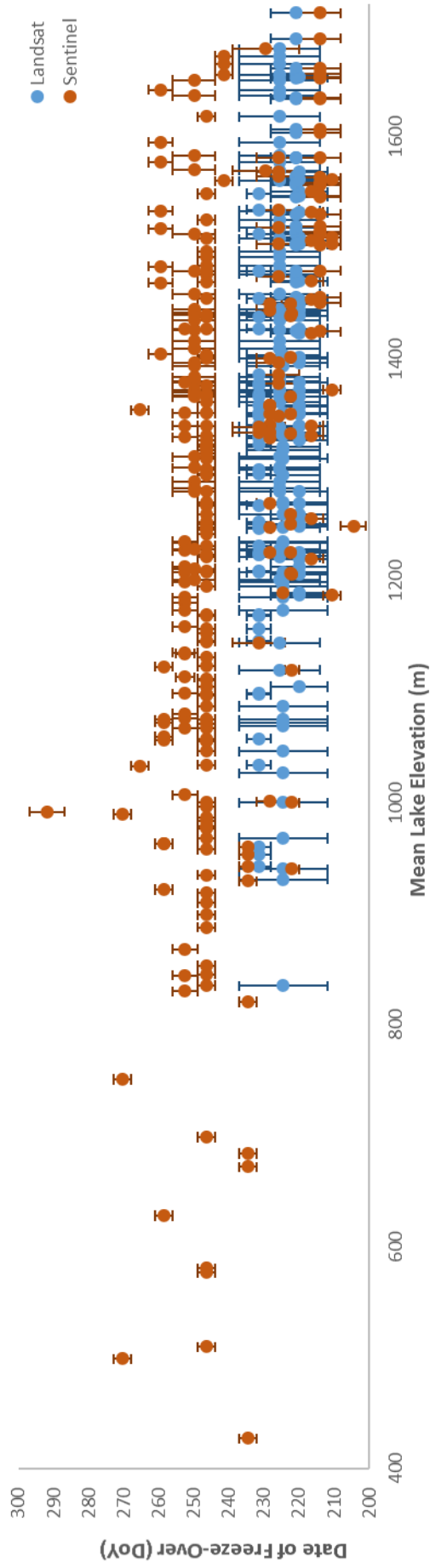


Figure 17 – Graph displaying the date of freeze-over for each lake against its mean elevation, with the error for each date shown by the error bars, as detected by the Landsat and the Sentinel data

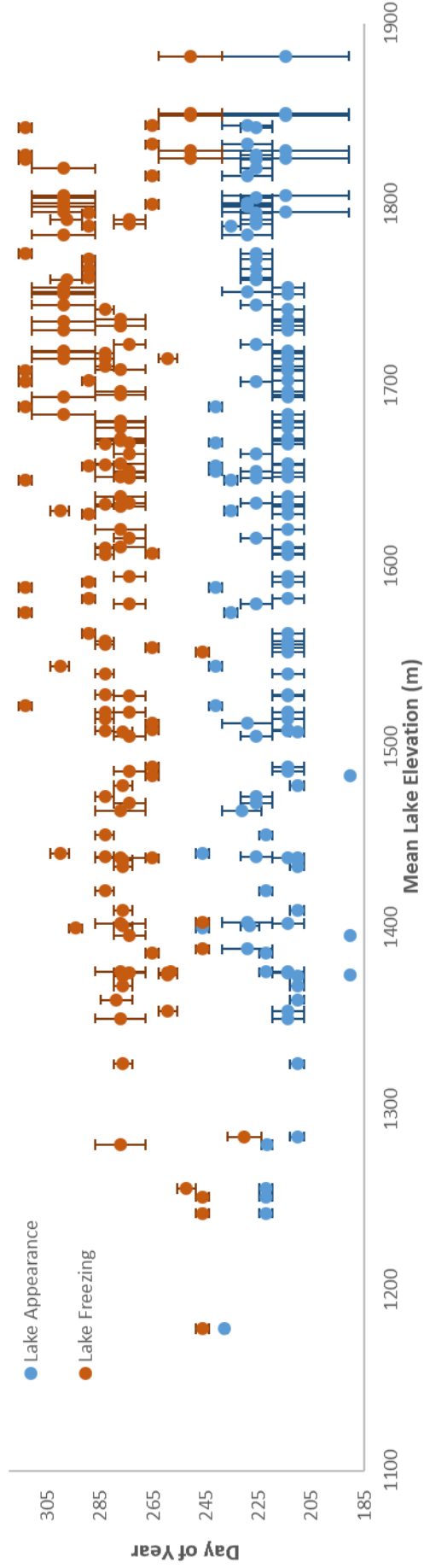


Figure 17 - Graph displaying the date of appearance and disappearance for each buried lake against its mean elevation, with the error for each date shown by the error bars, as detected by the Sentinel data

4.4 – Buried Lakes

The appearance and subsequent freezing dates (with errors) of the 150 buried lakes that were identified from the Sentinel imagery are mapped in Figure 18. Nine of the buried lakes at the highest elevations (all above 1789 m) were never visible in the Landsat imagery. The remainder were partially visible in the Landsat data as a result of slight melting around their perimeter, detectable as water by the NDWI classification. Any trend in buried lake appearance is difficult to decipher from Figure 18. South of Jakobshavn Isbræ, buried lakes at higher elevations generally appear later than those at lower elevations. However, north of Jakobshavn Isbræ the pattern is more complex, with a cluster of lakes appearing even later than those south of Jakobshavn Isbræ, while another cluster of lakes even further north appear much earlier. The same is true for the freezing and resultant disappearance of the buried lakes. The pattern south of Jakobshavn Isbræ is relatively clear, with lakes at lower elevations tending to freeze earlier (although even here there are anomalies, with several lakes at the highest elevations in the south freezing very early). The pattern of buried lake freeze-over north of Jakobshavn Isbræ is also similar to that shown by the appearance of these lakes: the cluster of lakes that appeared very late are present much longer than the lakes furthest north that appeared before this cluster. These weak relationships between buried lake appearance and freeze-over with elevation are corroborated by Figure 17, which shows these dates and their associated errors plotted against the mean lake elevation. There is a clearer trend between elevation and buried lake freezing (R^2 value of 0.16) than between elevation and buried lake appearance (R^2 value of 0.02), however, both trends are weak.

Imagery	Mean day (Day of Year)	Mean positive and negative error (± days)	Earliest and latest dates (Day of Year)	Mean lake area (min and max) (km ²)	Mean lake elevation (min and max) (m)
Lake Appearance	219.7	6.2	190.5 – 246.5	2.7 (0.1 – 15.9)	1606 (1179 – 1882)
Lake Freezing	280.6	5.9	230.5 – 313.5		

Table 6 - Statistics from the buried lake appearance and disappearance detections of the Sentinel data

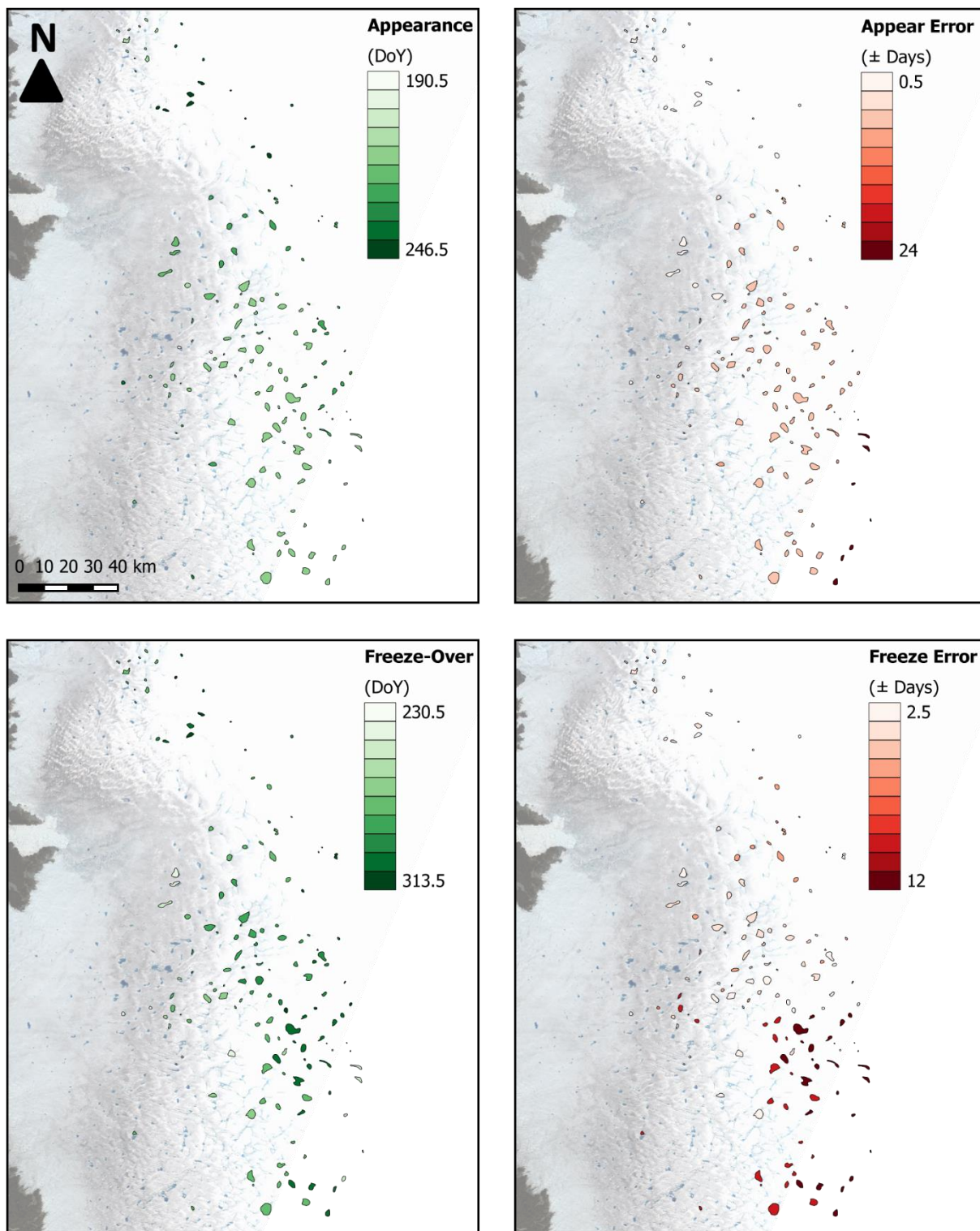


Figure 18 – Buried lake appearance (top row) and disappearance (bottom row) detections from the Sentinel data. The date of appearance/disappearance is mapped for each lake in the left-hand image, and the associated error for that date mapped in the right-hand image. The background image is a Landsat RGB false colour scene acquired on DoY 196

The errors in the dates shown in Figure 18 increase significantly for the appearance dates of the buried lakes at the highest elevations; this was due to there being a restricted number of Sentinel scenes that covered the highest elevations. This is also reflected in the mean error of buried lake appearance and disappearance dates (Table 6). The mean elevation of 1606 m for the buried lakes is significantly higher than the mean elevation of supraglacial lakes that froze at the end of the melt seasons (1249 m; Table 5), and the average lake size is almost double (2.7 km² for buried lakes, compared to 1.2 km² for freezing lakes; Table 5 and 6). The largest buried lake size detected (15.9 km²) is almost twenty times greater than the largest draining supraglacial lake and more than double the size of the largest supraglacial lake that froze over.

5. Discussion

5.1 – Lake Detection

Overall, the semi-automated method of lake detection from Sentinel images has been relatively successful. Lakes are very distinct in the majority of pre-processed Sentinel scenes (for example, in Figure 4), and the methodology has extracted lake areas with reasonable accuracy compared to the Landsat NDWI classification of lakes. Figure 9 shows that the individual lake areas detected by the Sentinel and the Landsat methods show a strong positive relationship for all three days that a contemporaneous image was available from both sensors. The R^2 values, all greater than 0.91 (Fig.9), suggest that the areas calculated from each image are comparable, i.e. that lake detection using Sentinel images produces lake areas within a reasonable accuracy of the Landsat NDWI lake detection. The graph of total lake area (Fig.12), disregarding the Sentinel anomalies of DoY 188, 190 and 244, shows the Sentinel lake area to follow a very similar trend to the Landsat through the summer, with the maximum lake areas being recorded on DoY 189 and 198, respectively. The results obtained through the previously un-investigated method of Sentinel-1 SAR detection of GrIS supraglacial lakes are therefore shown to be capable of producing similar results to the well-established method of Landsat NDWI lake classification.

The accuracy of Sentinel lake detection is further corroborated when compared to values presented by similar studies in the literature. The total maximum standardised lake area of 407.6 km² on DoY 189 for a total of 2297 detected lakes (Fig.13) is a suitable statistic to compare to similar values in the literature, although it is important to remember that this image covered only 60% of the full ~42,000 km² study area (Table 2), therefore this figure may be overestimated. Selmes et al. (2011) calculated a mean total lake area of 1036 ± 134 km² from 2005-2009 for the whole of southwest Greenland; a study area nearly three times the size in this study. Fitzpatrick et al. (2014) examined a much smaller study area of ~6,500 km² further south at Russell Glacier, finding a maximum lake area ranging from 158 km² in 2003, to 160 km² in 2012; while Johansson & Brown (2013) had a maximum lake area of 178

km² over their ~14,500 km² study region. The maximum lake extent calculated in this study using Sentinel imagery compares well to the values calculated in these studies; the latter two study regions were further south than the current study, therefore a greater lake area would be expected. The number of lakes detected by the Sentinel imagery in this study (2297) is greater than in all of these studies (1120; 200; 115 respectively), however, these studies utilised MODIS imagery and therefore discarded lakes smaller than 1-2 pixels (0.0625-0.125 km²). The number of lakes detected here is more comparable to that of Lampkin (2011), who delineated 1180 lakes using Landsat-7 over a study area approximately half the size of this study. Therefore, Sentinel imagery not only depicts supraglacial lakes with an accuracy that is comparable to Landsat NDWI classification, but can also accurately detect much smaller lakes than is possible with MODIS. This is further supported by the RMSE values (Table 3); Liang et al. (2012) state the RMSE value favours smaller lakes, while the RMSE/km² favours larger lakes. The RMSE values for DoY 212 and 237 are lower than equivalent values reported in the literature, supporting the better detection of smaller lakes in Sentinel imagery compared to MODIS. On DoY 189, the RMSE value is expected to be greater than DoY 212 and 237, as this image is closer in time to the maximum total lake area and therefore larger lakes are more likely to be present (rather than drained). Conversely, the RMSE/km² values in this study are larger than those in the literature stated for MODIS (Table 3), likely due to the greater suitability of MODIS for larger lake detection. The higher spatial resolution of Sentinel imagery compared to MODIS consequently makes it more suited to the detection of smaller supraglacial lakes.

However, when analysing the accuracy of the Sentinel lake detection method in finer detail, it is clear that the method overestimates lake area compared to the Landsat NDWI method (Fig.13). Figure 10 plots the difference in individual lake areas from the Sentinel and the Landsat against elevation, however, there is no determinable bias with elevation. At most, it can be concluded that the Sentinel method appears to significantly overestimate lake areas between ~1200 and 1400 m elevation on DoY 189. On inspection of the Landsat-8 false colour scenes, these elevations are at the upper end of a band of cryoconite and dirty ice, but are also relatively complex in topography due to the presence of slush zones, and thus a large amount of surface water during this time (shown in Fig.12D-F). Slush zones and cryoconite on

the ice surface would absorb the radar waves in a similar manner to the water in supraglacial lakes, reducing the backscatter and therefore producing a similar return to the lakes, erroneously increasing the area defined by the Sentinel imagery as lakes (Fig.8D-F). Johansson & Brown (2012), the only other comparable study using SAR to investigate supraglacial lakes on the GrIS, used winter imagery to avoid such an effect. It was due to this effect of the slush and cryoconite that the very initial test of a direct threshold value for the original Sentinel images was unsuccessful in detecting lakes, and the resultant Sentinel lake classification method (Fig.2) was only conducted within the areas defined by the dilated Landsat maximum lake extent mask. However, Figure 8D-F shows that this effect was not completely mitigated, and therefore further work is needed to improve the accuracy of lake area detection using Sentinel imagery. Similar complications have been overcome for lake detections using optical imagery, for example with cryoconite (Johansson & Brown 2013), therefore it is likely that a comparable procedure could be carried out for Sentinel lake detections.

The two Sentinel polarisations assessed in this study differ significantly in their ability to detect supraglacial lakes. In general, the HV polarisation is better at depicting lakes than the HH polarisation, detecting much greater areas that are comparable to the Landsat detections (Table 3). However, there are several days where the HH polarisation picks up a greater number of lakes than the HV (Fig.3), and very few days that the majority of the lake area is detected by both polarisations (Fig.11). Therefore, both polarisations were necessary to obtain the total lake areas used in this study. Dual polarisation, particularly HH and HV (rather than VV/VH), offers the ability to discriminate between the backscatter returns of ice and water, which can often be difficult due to the similar backscatter signature of these surfaces (Partington et al. 2010). While the signal-to-noise ratio of the HH polarisation is high and therefore less useful, the cross-polarised signal of the HV polarisation reduces the signal-to-noise ratio, producing a distinction between ice, snow, water and slush backscatter, even on steep surface slopes, for example near the ice sheet edge (Nagler et al. 2015; Nagler et al. 2016). This explains the presence of lakes in the HV polarisation when they have seemingly disappeared in the HH images (Fig.12D-F). Furthermore, the two polarisations are affected by differing environmental conditions, the most relevant of which is the presence of wind. Figure 12A-C shows consistently very high backscatter values for all the lakes in the HH polarisation,

despite these lakes being clearly present in the HV polarisation and Landsat false colour image. This is therefore interpreted as the effect of wind over this area of the ice sheet, due to the uniform backscatter pattern over the image (Fig.12B), and as the lakes have not drained (Fig.12A,C). The HV polarisation backscatter response from water is conversely unaffected by wind-induced surface roughness (Scheuchl et al. 2004), and therefore these lakes are still detected by the Sentinel lake detection due to the summing of the lake detections from each polarisation (Fig.2H). HV backscatter from ice is affected by surface roughness more than HH, explaining the small number of days shown in Figure 3 where a greater lake area is detected in the HH polarisation (Scheuchl et al. 2004). Therefore, analysis of the dual Sentinel polarisations allows the detection of lakes even when affected by environmental variables such as wind. Radar waves can also penetrate clouds, which are a substantial issue in the use of optical imagery causing many images to be discarded, providing a further advantage of the Sentinel imagery over optical sensors for supraglacial lake detection.

Although the Sentinel lake detection method presented has been shown to be reasonably successful compared to Landsat NDWI lake classification, a number of improvements are suggested that could further improve the accuracy of the Sentinel lake detections. First, it has been assumed that the Landsat-8 NDWI lake classification accurately depicts all lake areas. However, use of the red and blue bands was assumed best based on the only study that has currently used Landsat-8 to delineate supraglacial lakes (Pope et al. 2016); further investigation into alternative bandmath combinations could prove another method to be more accurate when compared with manually delimited lakes. Second, the decision to choose a single threshold value for all Landsat NDWI images may have resulted in an underestimation of some lake areas at the start and end of the melt season, where a lower threshold may have been more appropriate to detect the full extent of water presence. Coincidentally, the Sentinel lake detection method may not have overestimated the lake area as much as has been suggested, if the Landsat classification indeed underestimated the lake areas. A single Landsat threshold was deemed more appropriate due to the superimposition of the binary lake masks to create the Landsat maximum lake extent mask that was applied to the Sentinel images, but as individual thresholds were chosen for each Sentinel image, it is suggested that this may also be more appropriate for the Landsat NDWI images. Third, inclusion of an

additional form of imagery, such as ASTER or WorldView, could be used to validate the lake areas detected by the Sentinel, and would therefore allow improvements of the Sentinel lake detection thresholds, enhancing the accuracy of the final lake extents. Such a step is carried out in the majority of supraglacial lake detection studies, but it was not possible to validate the Sentinel lake areas using the Landsat imagery in this study due to the use of the Landsat within the methodology. Instead, the Sentinel lake detections were only carried out within the areas defined by the dilated Landsat maximum lake extent mask, and manual checking of the threshold values against the original images restricted the erroneous identification of water.

Fourth, a higher spatial resolution could be obtained for the Sentinel imagery if a higher resolution DEM was used in the pre-processing stages. An alternative swath mode of the Sentinel-1 satellites could even be used to produce a higher resolution DEM than the GETASSE30 DEM used in the current study: the Interferometric-Wide swath, with a 10 m resolution, has been designed to enable extremely detailed reconstructions of surface topography (Wegmüller et al. 2015). This could result in the Sentinel imagery having a superior spatial resolution than Landsat-8 imagery. Fifth, if areas of slush or cryoconite are known to be present and a more stringent thresholding technique is not successful in discriminating backscatter returns from these areas from those of lakes, these areas could be masked out from the Sentinel imagery within the pre-processing stages (Fig.2) to avoid any erroneous overestimation of lake areas, such as DoY 190 (Fig.13). Finally, whilst the 2-pixel dilation of the Landsat maximum lake extent mask appears to work well in defining lake extents with a small buffer of ice pixels to create the bimodal histogram distributions of the pixel values (Fig.2E,F), this stage disregards any change in the lake extents through the melt season. Subsequently, a large number of ice pixels can be picked up as lakes are forming, or after they have drained; which likely contributed to the concealment of the double peak of some less well-defined bimodal histogram distributions. This could be accounted for by a scaling of the lake dilation depending on the size of each lake throughout the season; this would be time-consuming to implement manually, but not if the method were automated. It is suggested that there is potential for the Sentinel lake detection method presented here to be automated, now that preliminary work has been carried out and shown to be reasonably

successful compared to the Landsat NDWI classifications. As the method stands, it is not deemed accurate enough to be able to fully replace optical imagery for lake detections, though it would certainly be useful as a supplement, for example where cloud cover reduces the temporal resolution of optical imagery. This same conclusion was reached by Johansson & Brown (2012), however, further to their conclusions, it is proposed here that if the improvements above are implemented and successful, lake detections using Sentinel-1 SAR images could be a suitable replacement for optical imagery.

5.2 – Lake Drainage

The rapid drainage detection algorithm, which utilised the lake areas detected from the Sentinel imagery and from the Landsat imagery, correctly identified a number of drainages. Significantly, the algorithm run using lakes detected by the Sentinel imagery found a much larger number of drainages (48) than the run using the Landsat-detected lakes (4; Table 4). This was primarily due to the higher temporal resolution of the Sentinel imagery, resulting in the detection of a greater number of drainage events, and also in a lower mean error associated with the drainage dates (± 0.7 compared to ± 1.0 for Sentinel and Landsat respectively; Table 4). Considering that only four drainages could be detected from the Landsat due to the infrequent repeat image acquisition, this ± 1.0 day error is unrepresentative of the true error that prevented a large number of drainages from being detected. The ± 0.7 day error for the Sentinel is very respectable, however, and is comparable to detections with MODIS imagery where images are acquired daily. The total of 48 drainages according to the Sentinel is also comparable to studies in the same region within the literature: Selmes et al. (2011) detected a mean of 160 ± 42 drainages a year between 2005-2009 over a study area ~ 3 times larger than the one in this study, while Box & Ski (2007) record 8 events a year over a much smaller area, but note that they miss a significant number of events due to the low spatial resolution of MODIS. In this study, only drainage events for lakes greater than 0.2 km^2 were assessed due to the volume of manual validation that was required, therefore the smallest lake size is comparable to that detectable in MODIS imagery.

Nevertheless, the Sentinel imagery also detected drainages for lakes significantly smaller than 0.2 km², and therefore smaller than can be detected by MODIS. Therefore, lake drainage detection using Sentinel imagery has substantial advantages over detection using either Landsat (i.e. more drainages can be detected) or MODIS imagery (smaller lake drainages can be detected).

The comparison of the four drainages detected by the Landsat imagery shows a more variable success of the Sentinel imagery in detecting rapid lake drainages, as the Sentinel imagery missed two of the drainages that the Landsat imagery detected. This is likely due to the thresholds implemented in the drainage algorithm, for example that a lake needed to lose over 80% of its area within 4 days to be registered as a drainage event; if a 79% decrease in lake area had been calculated, this would not have counted as a drainage. For the other two drainages that were detected by both the Landsat and Sentinel images, the predicted drainage dates are extremely close (almost within the error uncertainty), and the day of drainage can be even more accurately pinpointed by combining the dates obtained by the Landsat and Sentinel detections. This demonstrated a further advantage of the Sentinel imagery for detecting rapid lake drainages, as the more northerly of these two lakes (Fig.14) actually showed a two-part drainage, which was detected by the Sentinel imagery but not the Landsat. As all drainages were manually checked, the final total of drainage events does not include any erroneous drainages (Table 4). Although misidentification was an issue, the drainages due to 'no data' values can be overcome either within the drainage script or by re-processing the Sentinel images, therefore although this is a limitation of the current study, it is not seen as a disadvantage of the method. The Sentinel and the Landsat drainage detections also missed several drainages that were noted manually; this is suggested to be due to the irregular timing between the Sentinel images and large intervals between the Landsat images, resulting in these drainages lying outside of the implemented thresholds in the algorithm. This will not be a problem for any investigations in future summers using Sentinel imagery, as since early 2016 Sentinel-1B has also settled into a regular orbit following the Sentinel-1A satellite, resulting in a more regular image acquisition (every 2-3 days from January 2016). Furthermore, high resolution images are now always available, whereas for the first half of 2015, medium resolution was the highest available (Table 2). Therefore, there is substantial

potential for future use of Sentinel imagery to detect rapid supraglacial lake drainages on the GrIS.

Further improvements are suggested in order to improve the detection of supraglacial lake drainage using Sentinel imagery, in addition to an update of the drainage algorithm to encompass the potential presence of 'no data' values within lake basins. A temporal threshold at a set point of the melt season could be implemented in order to automatically differentiate between lake drainages and lakes that freeze-over towards the end of the melt season; this could be defined by manually, or through the inclusion of temperature data (with freeze-over defined as temperature dropping below zero degrees (Selmes et al. 2013)). Unfortunately, processed temperature for this region of the GrIS will not be available until later in 2016, but this could be investigated for future work. The script could therefore be expanded to include the detection of supraglacial lake freeze-over (see Section 5.3), but also slower lake drainages if the temporal threshold of 4 days was increased. Slower lake drainages may have a smaller impact on ice velocities than rapid drainages, but can still result in significant local speedups (Tedesco et al. 2013). However, if the temporal resolution is poor, rapid drainages could be incorrectly identified as slow drainages, rather than not being detected at all, therefore this would only be suitable for imagery with a high repeat acquisition rate, such as the Sentinel satellites. Drainage detection using Sentinel imagery therefore has advantages over detection using optical imagery, however, the method currently does not prove a viable replacement for optical imagery. Nevertheless, if alterations to both lake detections (Section 5.1) and drainage depiction as outlined above are successful, the method may have potential to pose a viable alternative method to optical imagery for supraglacial lake drainage detection.

5.3 – Lake Freeze-Over

Identification of supraglacial lake freeze-over towards the end of the melt season has been limited in the literature, partly due to the inability of optical sensors to image at this time of

year because of greater cloud presence and a decreasing amount of sunlight. These limitations are overcome by SAR sensors, which provide their own signals and can thus image in any light condition, while their microwave wavelengths are unaffected by cloud cover (Van Zyl & Kim 2011). This is demonstrated by the earlier freeze-over dates depicted from the Landsat imagery compared to Sentinel imagery (Table 5), as detection of the latest lake freeze-over dates in the Landsat was obscured by the presence of snowfall from DoY 228 (Fig.5). Subsequently, the mean freeze-over date for supraglacial lakes from the Landsat imagery is DoY 224.8 ± 8.3 days, whereas the Sentinel imagery puts this date substantially later on DoY 240.1 ± 3.7 (Table 5). This is a result of the Sentinel SAR being able to penetrate a shallow snow cover to return the backscatter signal of liquid water beneath, allowing a more accurate depiction of the freeze-over dates. However, *in situ* measurements are required in order to know exactly how far the Sentinel SAR waves penetrate into the snow cover. The greater temporal resolution of the Sentinel imagery also gave a mean error for the freeze-over dates that was 2.6 times smaller than for the dates obtained from the Landsat imagery (Table 5). Therefore, Sentinel imagery is considerably more suited to the detection of supraglacial lake freeze-over than optical imagery such as Landsat.

The mean elevation of lake freeze-over was 1249 m, which is strikingly similar to that reported in the Selmes et al. (2013) study of ~1500 m between 2005-2009. Additionally, they also find that the mean elevation of freezing lakes occurs ~200 m higher on the ice sheet than those lakes that drain, as was found in the current study (Tables 4 and 5), and that the mean lake size of lakes that freeze-over is greater than those that drain. Although their lake sizes are smaller than those in the current study (0.5 vs 0.2 km² compared to 1.2 vs 0.6 km² respectively; Table 5), the similar conclusions provide further confidence in the Sentinel detection of lake freeze-over dates. The smaller lake size of the Selmes et al. (2011) study is unexpected due to their use of MODIS imagery; however, caution has already been drawn to this figure for the Sentinel imagery as it was calculated from the maximum extent of the lakes, not the size at the point of freeze-over. This should be addressed in any future work utilising Sentinel imagery for lake freeze-over detection, and implementation of a minimum lake size threshold should be considered to avoid tiny lakes for which the backscatter signal was not distinct enough for a date to be accurately determined. Selmes et al. (2013) did not

investigate any further trend with elevation, yet Figures 15 and 16 show a weak downglacier trend in freezing, with the highest elevation lakes freezing first and lower elevation lakes later. It is suggested that this may be a result of colder air from higher on the ice sheet causing lakes at higher elevations to freeze earlier, while those at nearer the ice sheet margin are exposed to warmer temperatures due to a closer proximity to the ocean and greater presence of an insulating cloud cover. However, meteorological data is vital to justifying any such conclusions, as temperature is the most likely control on the timing of lake freeze-over (Selmes et al. 2013).

Regardless of the inconclusive relationship between lake freezing and elevation, the highest elevation of 1712 m for a freezing lake is significant. Sundal et al. (2009) found extremely few supraglacial lakes above 1600 m in 2003, yet from Figure 16 it can be seen that a substantial number of lakes present above 1600 m froze over. This upglacier trend in supraglacial lake formation has also been found by a significant number of studies in the literature, and has been linked to increasing surface temperatures, followed by an upglacier trend in lake drainage (Liang et al. 2012; Howat et al. 2013; Morriss et al. 2013; Fitzpatrick et al. 2014). Although the lakes in this study were detected to freeze-over rather than drain, their formation is significant, as if temperatures continue to increase, lakes at these elevations may begin to drain rather than freeze, therefore impacting ice velocities (Sole et al. 2011; Bartholomew et al. 2012; Doyle et al. 2014). Therefore, detection of supraglacial lake freeze-over using Sentinel could be utilised in terms of investigating future potential rapid lake drainages, and inferring the potential resultant impact on ice dynamics. Sentinel imagery is well suited to the detection of lake freeze-over, and as there is scope to automate the method (Section 5.2), it may be even more desirable for future analysis.

5.4 – Buried Lakes

The Sentinel imagery is also extremely well suited to the detection and areal calculation of buried lakes; both those that partly appear in the Landsat imagery (and thus a rough estimation could be made of area), but particularly truly buried lakes that are not at all visible in the Landsat imagery. The only other investigation of buried lakes in the literature utilised IceBridge Ice Penetrating Radar to assess the depth of buried lakes, but could not accurately detect the areal extent (Koenig et al. 2015). Conversely, the use of Sentinel imagery has allowed not only the calculation of lake area, but also a determination of the lifespan of these buried lakes. The mean day of appearance is DoY 219.7 ± 6.2 , while the mean day of disappearance is well beyond the end of the melt season on DoY 280.6 ± 5.9 (Table 6). In comparison with the supraglacial lakes detected in this study that either drain (mean DoY 190.7 ± 0.7 ; Table 4) or freeze (mean DoY 240.1 ± 3.7 ; Table 5), the buried lakes appear quite late in the melt season, except for a small number at lower elevations (Fig.18). The mean elevation of these buried lakes is substantially higher than the lakes which were detected to freeze-over, the elevations of which have already been discussed as significant (Section 5.3). The buried lakes extend up to nearly 1900 m, with an elevation range of 1179-1882 m (Table 6); Koenig et al. (2015) also find the majority of buried lakes to lie between 1000 and 2000 m and do not detect any above 2000 m. As discussed in Section 5.3, the ability to detect buried lakes could similarly be significant for future assessments of supraglacial lakes and potential drainages; as the mean and maximum buried lake size is significantly larger than the supraglacial lakes investigated in this study (Sections 5.2-3), these lakes are a small but important source of water in the GrIS hydrological budget (Koenig et al. 2015).

The study by Koenig et al. (2015) assumes that the meltwater contained in the buried lakes remains in a liquid form throughout the winter, however, the flight lines followed by the IceBridge Radar were erratic and only repeated in certain areas. By contrast, using the Sentinel imagery, the buried lakes have been shown to freeze through in the early winter, with the latest freezing occurring well into November (Table 6). As was noted for the draining and freezing lakes (Sections 5.2-3), there is only a very weak relationship between buried lake

appearance and disappearance with elevation, with the highest elevation lakes appearing and freezing latest (Fig.17). If not for the anomalous cluster of lakes furthest north in the study site, a trend in appearance could almost be suggested with distance north (Fig.18). However, this is not the case for freeze-over, where an elevational trend is more clear. The delayed freeze-over compared to supraglacial lakes discussed in Section 5.3 is suggested to be due to the insulating effect of snow cover present from late in the melt season. For a better understanding of the lifespan of these lakes, meteorological data such as temperature and snowfall would provide helpful insights. Therefore, although the Sentinel imagery provides limited information on why such lakes are present, it is extremely proficient at determining the lifespan of the buried lakes, which has not been examined in the literature.

The larger error bars for the freeze-over dates of buried lakes at the highest elevations, as a result of the lower number of available Sentinel images is a limitation of this study, but is not expected to be an issue for future use: as discussed in Section 5.1, now that the Sentinel satellites are in a regular orbit, image acquisition is now more regular than was available in 2015. Manual detection of the buried lakes is simple and arguably more straightforward than for supraglacial lakes in the summer, as there are no additional factors such as slush zones complicating the backscatter return for winter imagery (Johansson & Brown 2012). It is therefore suggested that there is substantial potential to automate this method in a similar way to the summer supraglacial lake detection using Sentinel imagery (Fig.2), but with a less complex methodology. As the backscatter return from the buried lakes tends to be more uniform across different images, one way to detect the lakes could be to average the pixel values within each lake and compare to the surrounding ice in order to compare whether the lake is present or not, similar to the moving-window pixel-comparison technique of Selmes et al. (2011). Whether detected manually or through an automated algorithm, lakes visible in Sentinel imagery can therefore be tracked through an entire year: summer and early winter have been demonstrated in this study, with the potential to extend later into the winter and into spring as the lakes reform again.

6. Conclusions

The overall aim of this study set out to investigate the ability of Sentinel SAR imagery to detect supraglacial lakes, and to elicit the spatial and temporal extent of lakes through an extended melt season. Only one study known to date has used SAR imagery to investigate supraglacial lakes on the GrIS (Johansson & Brown 2012), and none have utilised Sentinel SAR imagery. There were three key objectives, which will now be discussed in turn.

The first objective was to develop a lake detection method, beginning with raw unprocessed Sentinel images. The final method that was devised resulted in a binary classification of lakes for each Sentinel image, the accuracy of which was tested against the relatively well-established method of NDWI classification using Landsat-8 OLI imagery. Various techniques were evaluated, and although the final methodology is considerably more complex than the NDWI classification of Landsat imagery (Fig.2), it has been shown to be capable of producing comparable lake areas to the Landsat NDWI classification. A comparison of individual lake areas detected from the Sentinel and the Landsat imagery showed an extremely high positive linear correlation between the areas calculated by the two types of imagery (Fig.9). Additionally, although the total lake areas detected by the Sentinel were overestimated compared to those from the Landsat (Fig.13), the maximum total standardised lake area was in line with similar values in the literature (Selmes et al. 2011; Johansson & Brown 2013; Fitzpatrick et al. 2014). Due to the single threshold value chosen for all the Landsat imagery, it is suspected that the total lake area calculated by the Landsat may have been underestimated. The overestimation of Sentinel lake area is suggested to be due to the similar backscatter response of slush and cryoconite; although this effect was minimised by only thresholding Sentinel images within the dilated Landsat maximum lake extent mask, it was not completely overcome. However, with the implementation of additional thresholding procedures, such as those carried out for optical imagery (Johansson & Brown 2013), it is believed that this effect could be addressed in future work. Therefore, the methodology presented here for lake detection using Sentinel imagery has been shown to provide a reasonably accurate means for delineating supraglacial lakes on the GrIS.

Furthermore, the Sentinel lake detection was able to delimit lakes significantly smaller than is possible in MODIS imagery, which has a much lower spatial resolution (250 m, compared to 25 m for Sentinel). This is shown by the greater number of lakes detected by the Sentinel imagery compared to equivalent studies in southwest Greenland (Selmes et al. 2011; Lampkin 2011; Fitzpatrick et al. 2014). It is also demonstrated by the lower RMSE and higher RMSE/km² values from the individual lake areas in the current study compared to alternative studies using MODIS, supporting the better detection of smaller lakes in the Sentinel compared to MODIS (Selmes et al. 2011; Fitzpatrick et al. 2014). The dual polarisation capability of the Sentinel satellites also provides an additional advantage over optical sensor detection of supraglacial lakes. Not only can radar waves penetrate clouds, a major issue for optical sensors, but the HV polarisation is unaffected by environmental variables such as wind (Partington et al. 2010; Nagler et al. 2016), allowing for the discrimination of lakes from ice and slush in the Sentinel imagery in any weather condition. While the lake detection method presented has been shown to be successful when compared with Landsat NDWI thresholding, with some additional improvements such as an enhancement of the Sentinel imagery spatial resolution and of the lake thresholding technique, the method could produce comparable, or even superior results to the Landsat NDWI methodology. As there is also potential for the method presented here to be fully automated, it is concluded that lake detection from Sentinel imagery is an avenue that should be pursued in future research of GrIS supraglacial lakes.

The second objective was to explore the potential of the Sentinel imagery to detect supraglacial lake dynamics, namely rapid drainage and lake freeze-over through the melt season. The lake areas detected using both Landsat and Sentinel imagery were inputted into a rapid lake drainage detection script, which identified only 4 rapid drainages from the Landsat imagery, but 48 from the Sentinel data. This shows a significant advantage of the higher temporal resolution of the Sentinel imagery; due to smaller periods between images, more rapid drainage events were successfully identified with a lower mean error in the dates for each event (Table 4). The number of drainages detected was comparable to similar studies in the literature (e.g. Selmes et al. 2011), but this validation additionally showed that the Sentinel imagery is capable of detecting smaller lake drainages than with MODIS, the most

regularly used imagery due to its high temporal resolution. Although smaller lake drainages were not explicitly investigated here, the ability of the Sentinel lake detection method (Objective 1) to delimit significantly smaller lakes than MODIS imagery implies there is potential for the detection of much smaller drainages than is possible with MODIS. If the resolution of the Sentinel images can be improved during the pre-processing stages, it is possible that the detection of rapid lake drainages from the Sentinel imagery could also be superior to detection using Landsat imagery. Therefore, Sentinel imagery is valuable in the detection of lake dynamics in the form of rapid lake drainage, and holds significant potential for further extending this analysis with slight improvements to the methodology.

The assessment of Sentinel imagery in detecting supraglacial lake freeze-over towards the end of the melt season has also been successful. Identification of lake freeze-over in the literature has been limited, however, neither the lack of light nor greater presence of cloud that prevent optical sensors from imaging late in summer are an issue for SAR sensors, and the Sentinel imagery proved extremely well suited to pinpointing lake freeze-over. Additionally, the Sentinel SAR can penetrate thin snow covers that are present from late in the melt season, allowing more accurate dates to be obtained than was possible with Landsat imagery where these lakes were obscured by the snow. The temporal resolution again proved superior to the Landsat, producing a significantly smaller mean error for each freeze-over date, and it is suggested that there is potential to automate the detection of supraglacial lake freeze-over dates, possibly even within the rapid drainage detection algorithm. Therefore, the investigation of the second objective of this study has shown that Sentinel imagery has a significant capability for detecting supraglacial lake dynamics on an equivalent level to, but with the potential to become superior to, optical imagery.

The third objective was to extend the supraglacial lake analysis into the early winter, an even less investigated period in the literature due to the inability of optical sensors to image in semi-darkness. This allowed the discovery of buried supraglacial lakes as first detected by Koenig et al. (2015); however, while this study was only able to calculate the depth of buried lakes, use of the Sentinel imagery in the current study allowed a calculation of lake area and

the lifespan of these buried lakes. Buried lakes appear at much higher elevations on the ice sheet than the supraglacial lakes that were the focus of the rest of this study, and are often significantly larger in size and undetectable in visible imagery (Table 6; Fig.6). They also appear much later in the melt season, with some persisting well into November, which is suggested to be a result of snow on the surface providing an insulating layer from the colder temperatures at the surface (Fig.18). Investigation of supraglacial lakes in the early winter has therefore been proven successful, and as there is much potential for this method to be automated, analysis of lakes throughout the winter and early spring, where optical imagery is completely unavailable, could also be possible.

In conclusion, the ability of Sentinel imagery to detect and investigate the dynamics of supraglacial lakes on the GrIS has been shown to be extremely proficient. The detection of lakes using a semi-automated methodology produced almost comparable results to those from Landsat NDWI lake classification. With further improvements, this methodology could even prove to be superior to optical imagery, due to its higher spatial resolution than MODIS and better temporal resolution than Landsat. The same is true of the rapid drainage detection; the fully automated methodology was successful, and with amendments based on the limitations of this study, there is also significant potential for Sentinel imagery drainage detection to be superior to that of Landsat and MODIS. The detection of supraglacial lake freeze-over and buried lake appearance and disappearance using Sentinel imagery is a further advantage over optical imagery, which cannot image late enough in the year to detect such features due to the presence of cloud and lack of sunlight. Therefore, Sentinel imagery has been shown to successfully detect supraglacial lakes and investigate their dynamics through the summer and early winter, and with further work, this imagery could become a viable supplement, or even replacement, to optical imagery lake investigations. The findings of this study, particularly the determination of lake freeze-over dates and the calculation of buried lake areas and lifetimes which have not previously been evaluated, are important for GrIS hydrological research, and could help to better inform predictions of future sea-level rise contributions of the GrIS.

7. References

- Andrews, L.C. et al., 2014. Direct observations of evolving subglacial drainage beneath the Greenland Ice Sheet. *Nature*, 514(7520), pp.80–83.
- Ardhuin, F. et al., 2015. Estimates of ocean wave heights and attenuation in sea ice using the SAR wave mode on Sentinel-1A. *Geophysical Research Letters*, 42(7), pp.2317–2325.
- Arnold, N.S., Banwell, A.F. & Willis, I.C., 2014. High-resolution modelling of the seasonal evolution of surface water storage on the Greenland Ice Sheet. *The Cryosphere*, 8(4), pp.1149–1160.
- Bamber, J.L., Hardy, R.J. & Joughin, I., 2000. An analysis of balance velocities over the Greenland ice sheet and comparison with synthetic aperture radar interferometry. *Journal of Glaciology*, 46(152), pp.67–74.
- Banwell, A.F. et al., 2012. Modeling supraglacial water routing and lake filling on the Greenland Ice Sheet. *Journal of Geophysical Research: Earth Surface*, 117(4), pp.1–11.
- Banwell, A.F. et al., 2014. Supraglacial lakes on the Larsen B ice shelf, Antarctica, and at Paakitsoq, West Greenland: A comparative study. *Annals of Glaciology*, 55(66), pp.1–8.
- Banwell, A.F., Willis, I.C. & Arnold, N.S., 2013. Modeling subglacial water routing at Paakitsoq, W Greenland. *Journal of Geophysical Research: Earth Surface*, 118(February), pp.1282–1295.
- Bartholomew, T.C., Anderson, R.S. & Anderson, S.P., 2008. Response of glacier basal motion to transient water storage. *Nature Geoscience*, 1(1), pp.33–37.
- Bartholomew, I. et al., 2010. Seasonal evolution of subglacial drainage and acceleration in a Greenland outlet glacier. *Nature Geoscience*, 3(6), pp.408–411.
- Bartholomew, I. et al., 2012. Short-term variability in Greenland Ice Sheet motion forced by time-varying meltwater drainage: Implications for the relationship between subglacial drainage system behavior and ice velocity. *Journal of Geophysical Research: Earth Surface*, 117(3), pp.1–17.
- Bartholomew, I. et al., 2011. Supraglacial forcing of subglacial drainage in the ablation zone of the Greenland ice sheet. *Geophysical Research Letters*, 38(8), pp.1–5.
- Bindschadler, R. & Vornberger, P., 1992. Interpretation of SAR imagery of the Greenland Ice Sheet using coregistered TM imagery. *Remote Sensing of Environment*, 42(3), pp.167–175.
- Bindschadler, R.A. et al., 2013. Ice-sheet model sensitivities to environmental forcing and their use in projecting future sea level (the SeaRISE project). *Journal of Glaciology*, 59(214), pp.195–224.
- Bougamont, M. et al., 2014. Sensitive response of the Greenland Ice Sheet to surface melt drainage over a soft bed. *Nature Communications*, 5, p.5052.
- Box, J.E., 2013. Greenland ice sheet mass balance reconstruction. Part II: Surface mass

- balance (1840-2010). *Journal of Climate*, 26(18), pp.6974–6989.
- Box, J.E. & Ski, K., 2007. Remote sounding of Greenland supraglacial melt lakes: Implications for subglacial hydraulics. *Journal of Glaciology*, 53(181), pp.257–265.
- van den Broeke, M. et al., 2009. Partitioning recent Greenland mass loss. *Science*, 326(November), pp.984–986.
- Brown, L. & Young, K.L., 2006. Assessment of Three Mapping Techniques to Delineate Lakes and Ponds in a Canadian High Arctic Wetland Complex. *Arctic*, 59(3), pp.283–293.
- Catania, G.A. & Neumann, T.A., 2010. Persistent englacial drainage features in the Greenland Ice Sheet. *Geophysical Research Letters*, 37(2), pp.1–5.
- Catania, G.A., Neumann, T.A. & Price, S.F., 2008. Characterizing englacial drainage in the ablation zone of the Greenland ice sheet. *Journal of Glaciology*, 54(187), pp.567–578.
- Chandler, D.M. et al., 2013. Evolution of the subglacial drainage system beneath the Greenland Ice Sheet revealed by tracers. *Nature Geoscience*, 6(4), pp.1–4.
- Chen, W. et al., 2013. Improvement of glacial lakes detection under shadow environment using ASTER data in Himalayas, Nepal. *Chinese Geographical Science*, 23(2), pp.216–226.
- Chu, V.W., 2014. Greenland ice sheet hydrology: A review. *Progress in Physical Geography*, 38(1), pp.19–54.
- Colgan, W., Steffen, K., et al., 2011. An increase in crevasse extent, West Greenland: Hydrologic implications. *Geophysical Research Letters*, 38(18), pp.1–7.
- Colgan, W., Rajaram, H., et al., 2011. The annual glaciohydrology cycle in the ablation zone of the Greenland ice sheet: Part 1. Hydrology Model. *Journal of Glaciology*, 57(204), pp.697–709.
- Copernicus, 2016. Sentinels Scientific Data Hub. ESA. Available at: <https://scihub.copernicus.eu/> [Accessed February 1, 2016].
- Cowton, T. et al., 2013. Evolution of drainage system morphology at a land-terminating Greenlandic outlet glacier. *Journal of Geophysical Research: Earth Surface*, 118(1), pp.29–41.
- Csatho, B.M. et al., 2014. Laser altimetry reveals complex pattern of Greenland Ice Sheet dynamics. *Proceedings of the National Academy of Sciences of the United States of America*, 111(52), pp.18478–18483.
- Danielson, B. & Sharp, M., 2013. Development and application of a time-lapse photograph analysis method to investigate the link between tidewater glacier flow variations and supraglacial lake drainage events. *Journal of Glaciology*, 59(214), pp.287–302.
- Darnell, K.N. et al., 2013. The morphology of supraglacial lake ogives. *Journal of Glaciology*, 59(215), pp.533–544.
- Das, S. et al., 2008. Fracture propagation to the base of the Greenland Ice Sheet during supraglacial lake drainage. *Science*, 320(May), pp.778–781.

- Dow, C.F. et al., 2014. Upper bounds on subglacial channel development for interior regions of the Greenland ice sheet. *Journal of Glaciology*, 60(224), pp.1044–1052.
- Doyle, S. et al., 2014. Persistent flow acceleration within the interior of the Greenland ice sheet. *Geophysical Research Letters*, 41, pp.899–905.
- Doyle, S.H. et al., 2013. Ice tectonic deformation during the rapid in situ drainage of a supraglacial lake on the Greenland Ice Sheet. *Cryosphere*, 7(1), pp.129–140.
- Duguay, C.R. & Lafleur, P.M., 2003. Determining depth and ice thickness of shallow sub-Arctic lakes using space-borne optical and SAR data. *International Journal of Remote Sensing*, 1161(February), pp.475–489.
- Echelmeyer, K., Clarke, T.S. & Harrison, W.D., 1991. Surficial glaciology of Jakobshavn Isbrae, West Greenland: Part I. Surface Morphology. *Journal of Glaciology*, 37(127), pp.368–3825.
- Enderlin, E. et al., 2014. An improved mass budget for the Greenland Ice Sheet. *Geophysical Research Letters*, 41, pp.866–872.
- ESA, 2016. Sentinel-1 SAR. Available at: <https://sentinels.copernicus.eu/web/sentinel/user-guides/sentinel-1-sar> [Accessed June 20, 2016].
- Fahnestock, M. et al., 1993. Greenland Ice Sheet Surface Properties and Ice Dynamics from ERS-1 SAR Imagery. *Science*, 262(5139), pp.1530–1534.
- Fitzpatrick, A.A.W. et al., 2014. A decade (2002–2012) of supraglacial lake volume estimates across Russell Glacier, West Greenland. *The Cryosphere*, 8(1), pp.107–121.
- Fountain, A.G. & Walder, J.S., 1998. Water flow through temperate glaciers. *Reviews of Geophysics*, 36(97), p.299–328.
- Fricker, H. et al., 2007. An active subglacial water system in West Antarctica mapped from space. *Science*, 315(5818), pp.1544–1548.
- Gardelle, J., Arnaud, Y. & Berthier, E., 2011. Contrasted evolution of glacial lakes along the Hindu Kush Himalaya mountain range between 1990 and 2009. *Global and Planetary Change*, 75(1–2), pp.47–55.
- Georgiou, S. et al., 2009. Seasonal evolution of supraglacial lake volume from ASTER imagery. *Annals of Glaciology*, 50(52), pp.95–100.
- Gogineni, S. et al., 2014. Bed topography of Jakobshavn Isbræ, Greenland, and Byrd Glacier, Antarctica. *Journal of Glaciology*, 60(223), pp.813–833.
- Hall, D.K. et al., 2009. Evaluation of surface and near-surface melt characteristics on the Greenland ice sheet using MODIS and QuikSCAT data. *Journal of Geophysical Research: Earth Surface*, 114(4), pp.1–13.
- Hewitt, I.J., 2011. Modelling distributed and channelized subglacial drainage: The spacing of channels. *Journal of Glaciology*, 57(202), pp.302–314.
- Hirose, T. et al., 2008. Bottomfast ice mapping and the measurement of ice thickness on tundra lakes using C-band synthetic aperture radar remote sensing. *Journal of the*

- American Water Resources Association*, 44(2), pp.285–292.
- Hock, R. & Hooke, R.L., 1993. Evolution of the internal drainage system in the lower part of the ablation area of Storglaciaren, Sweden. *Geological Society of America Bulletin*, 105(4), pp.537–546.
- Hoffman, M.J. et al., 2011. Links between acceleration, melting, and supraglacial lake drainage of the western Greenland Ice Sheet. *Journal of Geophysical Research: Earth Surface*, 116(4).
- Holland, D.M. et al., 2008. Acceleration of Jakobshavn Isbræ triggered by warm subsurface ocean waters. *Nature Geoscience*, 1(10), pp.659–664.
- Holt, T.O. et al., 2014. The structural and dynamic responses of Stange Ice Shelf to recent environmental change. *Antarctic Science*, 26(06), pp.646–660.
- Howat, I.M. et al., 2013. Brief Communication “Expansion of meltwater lakes on the Greenland Ice Sheet.” *The Cryosphere*, 7(1), pp.201–204. Available at: <http://www.the-cryosphere.net/7/201/2013/>.
- Howat, I.M. et al., 2015. Brief communication: Sudden drainage of a subglacial lake beneath the Greenland Ice Sheet. *The Cryosphere*, 9(1), pp.103–108.
- Howat, I.M. et al., 2011. Mass balance of Greenland’s three largest outlet glaciers, 2000–2010. *Geophysical Research Letters*, 38(12), pp.1–5.
- Howat, I.M., Negrete, A. & Smith, B.E., 2014. The Greenland Ice Mapping Project (GIMP) land classification and surface elevation data sets. *The Cryosphere*, 8(4), pp.1509–1518.
- Hubbard, B. & Nienow, P., 1997. Alpine subglacial hydrology. *Quaternary Science Reviews*, 16(9), pp.939–955.
- Huggel, C. et al., 2002. Remote sensing based assessment of hazards from glacier lake outbursts: a case study in the Swiss Alps. *Canadian Geotechnical Journal*, 39(2), pp.316–330.
- Jawak, S.D. & Luis, A.J., 2014. A Semiautomatic Extraction of Antarctic Lake Features Using Worldview-2 Imagery. , (February 2016), pp.33–46.
- Jezek, K., Gogineni, P. & Shanableh, M., 1994. Radar Measurements of Melt Zones on the Greenland Ice Sheet. *Geophysical Research Letters*, 21(1), pp.33–36.
- Jezek, K.C. et al., 1993. Analysis of synthetic aperture radar data collected over the southwestern Greenland ice sheet. *Journal of Glaciology*, 39(131), pp.119–132.
- Jezek, K.C., 1999. Glaciological properties of the Antarctic ice sheet from RADARSAT-1 synthetic aperture radar imagery. *Annals of Glaciology*, 29, pp.286–290.
- Johansson, A.M. & Brown, I.A., 2013. Adaptive Classification of Supra-Glacial Lakes on the West Greenland Ice Sheet. *IEEE Journal of Selected Topics in Applied Earth Observations and Remote Sensing*, 6(4), pp.1998–2007.
- Johansson, A.M. & Brown, I.A., 2012. Observations of supra-glacial lakes in west Greenland using winter wide swath Synthetic Aperture Radar. *Remote Sensing Letters*, 3(6),

pp.531–539.

- Johansson, A.M., Jansson, P. & Brown, I.A., 2013. Spatial and temporal variations in lakes on the Greenland Ice Sheet. *Journal of Hydrology*, 476, pp.314–3205.
- Joughin, I. et al., 1996. A mini-surge on the Ryder Glacier, Greenland, observed by satellite radar interferometry. *Science*, 274(5285), pp.228–230.
- Joughin, I. et al., 2014. Brief communication: Further summer speedup of Jakobshavn Isbræ. *The Cryosphere*, 8(1), pp.209–214.
- Joughin, I. et al., 2010. Greenland flow variability from ice-sheet-wide velocity mapping. *Journal of Glaciology*, 56(197), pp.415–430.
- Joughin, I. et al., 2013. Influence of ice-sheet geometry and supraglacial lakes on seasonal ice-flow variability. *The Cryosphere*, 7(4), pp.1185–1192.
- Joughin, I. et al., 2008. Seasonal speedup along the western flank of the Greenland Ice Sheet. *Science*, 320(May), pp.781–783.
- Joughin, I., Abdalati, W. & Fahnestock, M., 2004. Large fluctuations in speed on Greenland's Jakobshavn Isbræ glacier. *Nature*, 432(7017), pp.608–610.
- Joughin, I.R., Winebrenner, D.P. & Fahnestock, M. a., 1995. Observations of ice-sheet motion in Greenland using satellite radar interferometry. *Geophysical Research Letters*, 22(5), pp.571–574.
- Kamb, B., 1987. Glacier surge mechanism based on linked cavity configuration of the basal water conduit system. *Journal of Geophysical Research*, 92(B9), pp.9083–9100.
- Koenig, L.S. et al., 2015. Wintertime storage of water in buried supraglacial lakes across the Greenland Ice Sheet. *The Cryosphere*, 9(4), pp.1333–1342.
- König, M., Winther, J.-G. & Isaksson, E., 2001. Measuring snow and glacier ice properties from satellite. *Reviews of Geophysics*, 39(1), pp.1–27.
- Krawczynski, M.J. et al., 2009. Constraints on the lake volume required for hydro-fracture through ice sheets. *Geophysical Research Letters*, 36(10), pp.1–5.
- Lampkin, D.J., 2011. Supraglacial lake spatial structure in western Greenland during the 2007 ablation season. *Journal of Geophysical Research: Earth Surface*, 116(4), pp.1–13.
- Lampkin, D.J. & Vanderberg, J., 2011. A preliminary investigation of the influence of basal and surface topography on supraglacial lake distribution near Jakobshavn Isbrae, western Greenland. *Hydrological Processes*, 25(21), pp.3347–3355.
- Leeson, A. et al., 2015. Supraglacial lakes on the Greenland ice sheet advance inland under warming climate. *Nature Climate Change*, 5(January), pp.51–55.
- Leeson, A.A. et al., 2013. A comparison of supraglacial lake observations derived from MODIS imagery at the western margin of the Greenland ice sheet. *Journal of Glaciology*, 59(218), pp.1179–1188.
- Leeson, A.A. et al., 2012. Simulating the growth of supraglacial lakes at the western margin of the Greenland ice sheet. *The Cryosphere*, 6(5), pp.1077–1086.

- Legarsky, J.J., Gogineni, S.P. & Akins, T.L., 2001. Focused synthetic aperture radar processing of ice-sounder data collected over the Greenland ice sheet. *IEEE Transactions on Geoscience and Remote Sensing*, 39(10), pp.2109–2117.
- Lettang, F.J. et al., 2013. Estimating the extent of drained supraglacial lakes on the Greenland Ice Sheet. *International Journal of Remote Sensing*, 34(13), pp.4754–4768.
- Lewis, S. & Smith, L., 2009. Hydrological drainage of the Greenland Ice Sheet. *Hydrological Processes*, 23, pp.2004–2011.
- Liang, Y.-L. et al., 2012. A decadal investigation of supraglacial lakes in West Greenland using a fully automatic detection and tracking algorithm. *Remote Sensing of Environment*, 123, pp.127–138.
- Livingstone, S.J. et al., 2013. Potential subglacial lake locations and meltwater drainage pathways beneath the Antarctic and Greenland ice sheets. *The Cryosphere*, 7(6), pp.1721–1740.
- Luckman, A. et al., 2014. Surface melt and ponding on Larsen C Ice Shelf and the impact of föhn winds. *Antarctic Science*, 26(6), pp.625–635.
- Luckman, A. & Murray, T., 2005. Seasonal variation in velocity before retreat of Jakobshavn Isbræ, Greenland. *Geophysical Research Letters*, 32(8), pp.1–4.
- Lüthje, M. et al., 2006. Modelling the evolution of supraglacial lakes on the west Greenland ice-sheet margin. *Journal of Glaciology*, 52(179), pp.608–618.
- Malenovský, Z. et al., 2012. Sentinels for science: Potential of Sentinel-1, -2, and -3 missions for scientific observations of ocean, cryosphere, and land. *Remote Sensing of Environment*, 120, pp.91–101.
- Mayaud, J.R. et al., 2014. Modeling the response of subglacial drainage at Paakitsoq, west Greenland, to 21st century climate change. *Journal of Geophysical Research: Earth Surface*, 119, pp.2619–2634.
- McMillan, M. et al., 2007. Seasonal evolution of supra-glacial lakes on the Greenland Ice Sheet. *Earth and Planetary Science Letters*, 262(3-4), pp.484–492.
- Meierbachtol, T., Harper, J. & Humphrey, N., 2013. Basal Drainage System Response to Increasing Surface Melt on the Greenland Ice Sheet. *Science*, 341, pp.777–780.
- Moon, T. et al., 2014. Distinct patterns of seasonal Greenland glacier velocity. *Geophysical Research Letters*, 41, pp.7209–7216.
- Moon, T. & Joughin, I., 2008. Changes in ice front position on Greenland's outlet glaciers from 1992 to 2007. *Journal of Geophysical Research: Earth Surface*, 113(2), pp.1–10.
- Morriss, B.F. et al., 2013. A ten-year record of supraglacial lake evolution and rapid drainage in West Greenland using an automated processing algorithm for multispectral imagery. *The Cryosphere*, 7(6), pp.1869–1877.
- Muckenhuber, S., Korosov, A.A. & Sandven, S., 2016. Open-source feature-tracking algorithm for sea ice drift retrieval from Sentinel-1 SAR imagery. *The Cryosphere*, 10(2), pp.913–925.

- Nagler, T. et al., 2016. Advancements for Snowmelt Monitoring by Means of Sentinel-1 SAR. *Remote Sensing*, 8(4), p.348.
- Nagler, T. et al., 2015. The Sentinel-1 Mission: New Opportunities for Ice Sheet Observations. *Remote Sensing*, 7(7), pp.9371–9389.
- Nakamura, K. et al., 2006. Sea-ice thickness retrieval in the Sea of Okhotsk using dual-polarization SAR data. *Annals of Glaciology*, 44, pp.261–268.
- Nghiem, S. V. & Bertoia, C., 2001. Study of Multi-Polarization C-Band Backscatter Signatures for Arctic Sea Ice Mapping with Future Satellite SAR. *Canadian Journal of Remote Sensing*, 27(5), pp.387–402.
- Nick, F.M. et al., 2013. Future sea-level rise from Greenland's main outlet glaciers in a warming climate. *Nature*, 497(7448), pp.235–80.
- Nienow, P., Sharp, M. & Willis, I., 1998. Seasonal changes in the morphology of the subglacial drainage system, Haut Glacier d'Arolla, Switzerland. *Earth Surface Processes and Landforms*, 23(9), pp.825–843.
- Nolan, M. et al., 2002. Analysis of lake ice dynamics and morphology on Lake El'gygytgyn, NE Siberia, using synthetic aperture radar (SAR) and Landsat. *Journal of Geophysical Research*, 108(D2), pp.1–12.
- Palmer, S. et al., 2011. Seasonal speedup of the Greenland Ice Sheet linked to routing of surface water. *Earth and Planetary Science Letters*, 302(3-4), pp.423–428.
- Palmer, S., McMillan, M. & Morlighem, M., 2015. Subglacial lake drainage detected beneath the Greenland ice sheet. *Nature Communications*, 6(8408).
- Palmer, S.J. et al., 2013a. Greenland subglacial lakes detected by radar. *Geophysical Research Letters*, 40(23), pp.6154–6159.
- Palmer, S.J. et al., 2013b. Greenland subglacial lakes detected by radar. *Geophysical Research Letters*, 40(23), pp.6154–6159.
- Partington, K.C. et al., 2010. Dual-polarization C-band radar observations of sea ice in the Amundsen Gulf. *IEEE Transactions on Geoscience and Remote Sensing*, 48(6), pp.2685–2691.
- Podrasky, D. et al., 2012. Outlet glacier response to forcing over hourly to interannual timescales, Jakobshavn Isbræ, Greenland. *Journal of Glaciology*, 58(212), pp.1212–1226.
- Pope, A. et al., 2016. Estimating supraglacial lake depth in West Greenland using Landsat 8 and comparison with other multispectral methods. *The Cryosphere*, 10, pp.15–27.
- Pritchard, H. et al., 2005. Glacier surge dynamics of Sortebræ, east Greenland, from synthetic aperture radar feature tracking. *Journal of Geophysical Research: Earth Surface*, 110(3), pp.1–13.
- Rennermalm, A.K. et al., 2013. Evidence of meltwater retention within the Greenland ice sheet. *The Cryosphere*, 7(5), pp.1433–1445.

- Rignot, E. et al., 2011. Acceleration of the contribution of the Greenland and Antarctic ice sheets to sea level rise. *Geophysical Research Letters*, 38(L05503), pp.1–5.
- Rignot, E., Echelmeyer, K. & Krabill, W.B., 2001. Penetration depth of interferometric synthetic aperture radar signals in snow and ice. *Geophysical Research Letters*, 28(18), pp.3501–3504.
- Rignot, E., Jezek, K. & Sohn, H., 1995. Ice flow dynamics of the greenland ice sheet from SAR interferometry. *Geophysical Research Letters*, 22(5), pp.575–578.
- Rignot, E. & Kanagaratnam, P., 2006. Changes in the Velocity Structure of the Greenland Ice Sheet. *Science*, 311(February), pp.986–991.
- Robin, G. de Q., Swithinbank, C.W.M. & Smith, B.M.E., 1970. Radio echo exploration of the Antarctic ice sheet. *International Association of Scientific Hydrology Publication*, 86, pp.97–115.
- Rott, H. & Mätzler, C., 1987. Possibilities and limits of synthetic aperture radar for snow and glacier surveying. *Annals of Glaciology*, 9, pp.195–199.
- Scheuchl, B. et al., 2004. Potential of RADARSAT-2 data for operational sea ice monitoring. *Canadian Journal of Remote Sensing*, 30(3), pp.448–461.
- Schoof, C., 2010. Ice-sheet acceleration driven by melt supply variability. *Nature*, 468(7325), pp.803–6.
- Selmes, N., Murray, T. & James, T.D., 2013. Characterizing supraglacial lake drainage and freezing on the Greenland Ice Sheet. *The Cryosphere Discussions*, 7(1), pp.475–505.
- Selmes, N., Murray, T. & James, T.D., 2011. Fast draining lakes on the Greenland Ice Sheet. *Geophysical Research Letters*, 38(15), pp.1–5.
- Sergienko, O. V., 2013. Glaciological twins: Basally controlled subglacial and supraglacial lakes. *Journal of Glaciology*, 59(213), pp.3–8.
- Shepherd, A. et al., 2009. Greenland ice sheet motion coupled with daily melting in late summer. *Geophysical Research Letters*, 36(1), pp.2–5.
- Siegert, M.J. et al., 2005. A revised inventory of Antarctic subglacial lakes. *Antarctic Science*, 17(03), p.453.
- Smith, D.M., 1996. Speckle reduction and segmentation of Synthetic Aperture Radar images. *International Journal of Remote Sensing*, 17(11), pp.2043–2057.
- Smith, L.C. et al., 2015. Efficient meltwater drainage through supraglacial streams and rivers on the southwest Greenland ice sheet. *Proceedings of the National Academy of Sciences of the United States of America*, 112(4), pp.1001–6.
- Sneed, W.A. & Hamilton, G.S., 2007. Evolution of melt pond volume on the surface of the Greenland Ice Sheet. *Geophysical Research Letters*, 34(3), pp.4–7.
- Sole, A. et al., 2013. Winter motion mediates dynamic response of the Greenland Ice Sheet to warmer summers. *Geophysical Research Letters*, 40(15), pp.3940–3944.
- Sole, A.J. et al., 2011. Seasonal speedup of a Greenland marine-terminating outlet glacier

- forced by surface melt-induced changes in subglacial hydrology. *Journal of Geophysical Research: Earth Surface*, 116(3), pp.1–11.
- Stevens, L.A. et al., 2015. Greenland supraglacial lake drainages triggered by hydrologically induced basal slip. *Nature*, 522, pp.73–76.
- Sundal, A. V. et al., 2009. Evolution of supra-glacial lakes across the Greenland Ice Sheet. *Remote Sensing of Environment*, 113(10), pp.2164–2171.
- Sundal, A.V. et al., 2011. Melt-induced speed-up of Greenland ice sheet offset by efficient subglacial drainage. *Nature*, 469(7331), pp.521–524.
- Tedesco, M. et al., 2013. Ice dynamic response to two modes of surface lake drainage on the Greenland ice sheet. *Environmental Research Letters*, 8, p.034007.
- Tedesco, M. et al., 2012. Measurement and modeling of ablation of the bottom of supraglacial lakes in western Greenland. *Geophysical Research Letters*, 39(2), pp.1–5.
- Tedesco, M. & Steiner, N., 2011. In-situ multispectral and bathymetric measurements over a supraglacial lake in western Greenland using a remotely controlled watercraft. *The Cryosphere*, 5(2), pp.445–452.
- Tedstone, A.J. et al., 2015. Decadal slowdown of a land-terminating sector of the Greenland Ice Sheet despite warming. *Nature*, 526(7575), pp.692–695.
- Tedstone, A.J. et al., 2014. Greenland ice sheet annual motion insensitive to spatial variations in subglacial hydraulic structure. *Geophysical Research Letters*, 41(24), pp.8910–8917.
- Tedstone, A.J. et al., 2013. Greenland ice sheet motion insensitive to exceptional meltwater forcing. *Proceedings of the National Academy of Sciences of the United States of America*, 110(49), pp.19719–24.
- Thomas, R.H. et al., 2003. Investigation of surface melting and dynamic thinning on Jakobshavn Isbrae, Greenland. *Journal of Glaciology*, 49, pp.231–239.
- Torres, R. et al., 2012. GMES Sentinel-1 mission. *Remote Sensing of Environment*, 120, pp.9–24.
- USGS, 2016. EarthExplorer. Available at: <http://earthexplorer.usgs.gov> [Accessed February 1, 2016].
- Vaughan, D.G. et al., 2013. Observations: Cryosphere. In T. F. Stocker et al., eds. *Climate Change 2013: The Physical Science Basis. Contribution of Working Group I to the Fifth Assessment Report of the Intergovernmental Panel on Climate Change*. Cambridge, United Kingdom and New York, NY, USA: Cambridge University Press, pp. 317–382.
- van der Veen, C.J., 2007. Fracture propagation as means of rapidly transferring surface meltwater to the base of glaciers. *Geophysical Research Letters*, 34(1), pp.1–5.
- Vornberger, P.L. & Bindshadler, R.A., 1992. Multi-spectral analysis of ice sheets using co-registered SAR and TM imagery. *International Journal of Remote Sensing*, 13(4), pp.637–645.

- van de Wal, R. et al., 2008. Large and rapid melt-induced velocity changes in the ablation zone of the Greenland Ice Sheet. *Science*, 321(July), pp.111–114.
- Van de Wal, R.S.W. et al., 2015. Self-regulation of ice flow varies across the ablation area in south-west Greenland. *The Cryosphere*, 9(2), pp.603–611.
- Wang, Z. et al., 2015. Multichannel Wideband Synthetic Aperture Radar for Ice Sheet Remote Sensing: Development and the First Deployment in Antarctica. *IEEE Journal of Selected Topics in Applied Earth Observations and Remote Sensing*, 9(3), pp.980–993.
- Wegmüller, U. et al., 2015. Sentinel-1 IWS mode support in the GAMMA software. In *Synthetic Aperture Radar (AP SAR), 2015 IEEE 5th Asia-Pacific Conference on*. pp. 431–436.
- Wingham, D.J. et al., 2006. Rapid discharge connects Antarctic subglacial lakes. *Nature*, 440(7087), pp.1033–1036.
- Xiaoqing, W. et al., 2013. Tomographic Observation and Bedmapping of Glaciers in western Greenland with IceBridge sounding radar. In *IEEE International Geoscience and Remote Sensing Symposium, 21-26 July 2013, Melbourne, Australia*. pp. 1–4.
- Xu, H., 2006. Modification of normalised difference water index (NDWI) to enhance open water features in remotely sensed imagery. *International Journal of Remote Sensing*, 27(14), pp.3025–3033.
- Yang, K. & Smith, L.C., 2013. Supraglacial streams on the Greenland Ice Sheet delineated from combined spectral-shape information in high-resolution satellite imagery. *IEEE Geoscience and Remote Sensing Letters*, 10(4), pp.801–805.
- Zwally, H.J. et al., 2002. Surface melt-induced acceleration of Greenland Ice-Sheet flow. *Science*, 297(5579), pp.218–222.
- Van Zyl, J. & Kim, Y., 2011. *Synthetic Aperture Radar Polarimetry*, Hoboken, NJ, USA: John Wiley & Sons.